A Complete HSS-Based Impedance Model of MMC Considering Grid Impedance Coupling

Zigao Xu, *Student Member, IEEE*, Binbin Li, *Member, IEEE*, Linjie Han, Junlin Hu, Shengbo Wang, *Student Member, IEEE*, Shiguang Zhang, and Dianguo Xu, *Fellow, IEEE*

***Abstract*—Harmonic state space (HSS) is seen as an effective impedance modeling method to precisely characterize the internal harmonic features of the modular multilevel converter (MMC). However, the existing MMC impedance models assume the ideal grid, ignoring the grid impedance, and they also do not incorporate the widely used dual-loop control and phase-locked loop (PLL). In this article, a complete MMC impedance model based on HSS is proposed to reveal the grid impedance coupling effect of MMC. The model analysis results demonstrate that the MMC impedance is coupled with the grid impedance due to the internal harmonics. This coupling causes MMC to be affected by the grid impedance and may cause instability. On the other hand, the proposed model not only consists of the ac current and the circulating current control, but also incorporates dc voltage outer loop and PLL with a clear physical meaning. Based on the proposed model, this article illustrates the factors that will enhance the coupling, which shows that the proposed model has to be used to improve the accuracy of the analysis. Finally, effectiveness of the proposed model is verified by simulation and experimental results.**

***Index Terms*—Dual-loop controller, grid impedance coupling, harmonic state space (HSS), modular multilevel converters (MMC), phase-locked loop (PLL).**

NOMENCLATURE[1]

j	Denotes three phases A, B, and C.
u/l	Denotes the upper or lower arm of MMC.
cm/dm	Denotes the common- or differential-mode (CM or DM) component.
N	Number of submodules per arm.
C	Submodule (SM) capacitance.
L	Arm inductance.
R	Parasitic arm resistance.
$Z_{\mathrm{gdc/ac}}(\omega)$	Equivalent impedance of dc/ac grid.
$u_{Z\mathrm{gdc/ac}j}(t)$	Voltage on dc/ac grid impedance.
$u_{\mathrm{gdc/ac}j}(t)$	Equivalent source voltage of dc/ac grid.
$u_{\mathrm{dc/ac}j}(t)$	DC/AC terminal voltage of MMC.
$i_{\mathrm{dc/ac}j}(t)$	DC/AC current of MMC.
$u_{\mathrm{u/l}j}(t)$	Arm voltages of MMC.
$i_{\mathrm{u/l}j}(t)$	Arm currents of MMC.
$u_{\mathrm{Cu/l}j}(t)$	SM capacitor voltages.
$i_{\mathrm{Cu/l}j}(t)$	SM capacitor currents.
$m_{\mathrm{u/l}j}(t)$	Arm modulation indexes.
$u_{\mathrm{N'N}}(t)$	Voltage between dc and ac grid neutral points.
$u_{\mathrm{cm/dm}j}(t)$	CM/DM arm voltages.
$i_{\mathrm{cm/dm}j}(t)$	CM/DM arm currents, where CM current is circulating current.
$u_{\mathrm{Ccm/dm}j}(t)$	CM/DM capacitor voltages.
$i_{\mathrm{Ccm/dm}j}(t)$	CM/DM capacitor currents.
$m_{\mathrm{cm/dm}j}(t)$	CM/DM modulation indexes.
$i^0_{\mathrm{cm}}(t)$	Zero-sequence components of circulating current.
$i^{\pm}_{\mathrm{ac}}(t)$	Positive- and negative-sequence components of ac current.
$\mathbf{i}_{\mathrm{cm}}$	Toeplitz matrix of circulating current.
$\mathbf{i}_{\mathrm{ac}}$	Toeplitz matrix of ac current.
$\mathbf{u}_{\mathrm{Ccm/dm}}$	Toeplitz matrixes of capacitor voltages.
$\mathbf{m}_{\mathrm{cm/dm}}$	Toeplitz matrixes of modulation indexes.
$\mathbf{Z}_{\mathrm{gdc/ac}}(\omega)$	Impedance matrix of dc/ac grid.
$\Delta\mathbf{S}(\omega)$	Coefficient matrix of the derivative in HSS.
$\Delta\mathbf{i}_{\mathrm{cm}}(\omega)$	Vector of circulating current perturbation.
$\Delta\mathbf{i}_{\mathrm{ac}}(\omega)$	Vector of ac current perturbation.
$\Delta\mathbf{u}_{\mathrm{Ccm/dm}}(\omega)$	Vector of capacitor voltage perturbations.
$\Delta\mathbf{i}_{\mathrm{Ccm/dm}}(\omega)$	Vector of capacitor current perturbations.
$\Delta\mathbf{m}_{\mathrm{cm/dm}}(\omega)$	Vector of modulation index perturbations.
$\mathbf{E}^s_+$, $\mathbf{E}^s_-$, $\mathbf{E}^s_0$	Sequence extraction matrixes, $s\in\{+,-,0\}$.
$\mathbf{T}_{\mathrm{dw}}$, $\mathbf{T}_{\mathrm{up}}$	Frequency downshift and upshift matrixes.

Manuscript received October 5, 2019; revised January 17, 2020 and April 1, 2020; accepted May 19, 2020. Date of publication May 21, 2020; date of current version July 31, 2020. This work was supported in part by the National Key Research and Development Program of China under Grant 2018YFB0904600, in part by the National Natural Science Foundation of China under Grant 51720105008, and in part by the Fundamental Research Funds for the Central Universities. Recommended for publication by Associate Editor Y. Tang. *(Corresponding author: Binbin Li.)*

The authors are with the School of Electrical Engineering and Automation, Harbin Institute of Technology, Harbin 150001, China (e-mail: orangesonhigh@163.com; libinbin@hit.edu.cn; linjie_han@163.com; 15395623201@163.com; wangshengbo1206@163.com; shiguang096@163.com; xudiang@hit.edu.cn).

Color versions of one or more of the figures in this article are available online at https://ieeexplore.ieee.org.

Digital Object Identifier 10.1109/TPEL.2020.2996714

[1]In this article, the expressions of some variables have removed "(t)" and "(ω)" to simplify the presentation style. For example, $u_{\mathrm{gdc}}(t)$ would be simplified as t_{gdc}, and $\Delta\mathbf{i}_{\mathrm{cm}}(\omega)$ would be simplified as $\Delta\mathbf{i}_{\mathrm{cm}}$.

I. INTRODUCTION

WITH advantages, such as scalable structure, high efficiency, and lower voltage distortion, the modular multilevel converter (MMC) [1]–[3] has attracted extensive attention in the field of high-voltage direct current (HVdc) transmission [4], [5]. However, many existing MMC-HVdc projects have been reported unstable phenomenon in a wide frequency range, from subsynchronous oscillation [6] to high-frequency oscillation [7]. These problems have prompted MMC modeling and stability analysis as a research hotspots in recent years [8], [9]. Among

the modeling techniques, the impedance model can reflect the dynamic relationship of terminal voltage and current, which has been widely used in the stability analysis of interconnected systems [10], [11].

The difficulty of MMC impedance modeling is mainly due to two factors. One is the time variance introduced by its internal harmonics, such as ripples of the circulating current and the submodule (SM) capacitor voltage [12]. The other factor is the nonlinearity caused by the closed-loop control, where the feedback variables multiplied with other state variables result in quadratic nonlinear terms. Some nonlinear operations in controllers, such as phase-locked loop (PLL) will also introduce nonlinearities into the model [13]. To deal with time variance and nonlinearity, a linearized MMC model in the *dq* frame is established in [14] by neglecting the harmonics of circulating current and capacitor voltage. But this simplification cannot reflect the interaction among different harmonics in MMC.

The harmonic state space (HSS) theory [15]–[17], which states that the model with signals varying periodically is possible to be linearized by means of Fourier series, is an effective way to deal with time-varying harmonics by transforming them from the time domain to frequency domain. This method was initially used to describe the modulation harmonics of the two-level converter [18]–[20] and further applied in the MMC modeling applications. Jamshidifar and Jovcic [21] and Sun and Liu [22], respectively, advocated the use of multiple-*dq* frames and multiple-harmonic linearization to model the MMC, which are considered to be essentially the same as HSS method because they all work by transforming MMC harmonics into the frequency domain [23]–[24]. Later on, the voltage controller [25], the zero-sequence (ZS) voltage compensation [26], the reduction-order method [27], and MMC dc impedance [28], [29] are gradually being developed with HSS-based MMC models. However, most of these modeling procedures assume an ideal grid and thus cause inaccuracy when MMC is connected to a grid with certain impedance. The grid impedance has been considered in the models of two-level converters [30]–[32]. It shows that the converter ac impedance will be affected by the connected grid impedance due to the filter capacitor in the dc link or the asymmetric control structure in the *dq* frame, which is named as the grid impedance coupling. In [24] and [25], the external impedance has been considered into the MMC modeling process, but the mechanism of the impedance coupling effect is not focused. Recently, although a small amount of literature mentions that the coupling exists in MMC ac side [33], a detailed analysis of this phenomenon has not yet been developed. Unlike the two-level converter, there is no filter capacitor on the MMC dc side, yet the grid impedance coupling still appears in MMC; and this coupling occurs not only on the ac side but also on the dc side.

On the other hand, the dual-loop control structure and the PLL are commonly used in the practical MMC-HVdc projects. Nevertheless, the models derived in [21]–[27] only consider the ac current/voltage single loop and the circulating current controller while they neglect the dc voltage outer loop and the PLL. The work presented in [28] and [29] include the dual-loop control but still without PLL, and the modeling procedure are not detailed. Sun and Liu [22] and Bessegato *et al*. [34] introduced the PLL into the MMC model and then analyzed the influence of phase angle dynamic on the Park and inverse Park transformation (PT and IPT) of MMC controllers. However, the frequency shift effect of PT and IPT is addressed by setting different controller transfer functions according to the sequence of the MMC variables, which makes the model mathematically complex and difficulty to find the physical meaning.

In this article, starting from the physical principle of the MMC circuit, a thorough analysis of the internal frequency coupling is presented in detail; subsequently, a complete HSS-based MMC impedance model is proposed. The impedance of the grid is taken into account during the modeling procedure, and thus the resulting model can exactly reveal the MMC grid impedance coupling effect. According to the proposed model, this article elaborates on the mechanism of this coupling, and points out that the MMC internal harmonic interaction is the key reason for it. Moreover, besides the ac current inner loop and the circulating current control loop, the dc voltage outer loop and the PLL are also modeled in HSS and connected with the open-loop MMC model to constitute the dual-loop structure. Based on the closed-loop model, the influences of MMC controllers and the weak grid on the grid impedance coupling are illustrated, which show that the proposed model has to be used to improve the accuracy of the analysis. In addition, this article introduces a frequency shift matrix and a sequence extraction matrix to reflect the frequency shift effect and the influence of PT and IPT on different sequences, respectively. These two matrixes make the HSS modeling for MMC controllers more concise with clear physical meaning.

The remainder of this article is organized as follows. The circuit and the time-domain model of MMC are presented in Section II. In Section III, MMC is linearized in HSS to get the open-loop impedance of ac and dc sides, respectively, and then the sequence of small-signal responses in MMC is analyzed. Furthermore, in Section IV, controllers are modeled in HSS to derive the closed-loop impedance of MMC, and the influence factors on the grid impedance coupling are also discussed. Then, the proposed model is demonstrated by simulation and experimental results in Section V. Finally, Section VI concludes this article.

II. MMC Model in Time Domain

The time-domain model is the basis for linearization. This section first devotes to obtaining the time-domain model of MMC from its three-phase circuit. Then, the model is simplified into single phase form to reduce order.

A. Circuit and the Three-Phase Model in Time Domain

The circuit configuration of MMC is presented in Fig. 1. It contains six arms, and each arm consists of *N* SMs plus an arm inductance *L* and a parasitic resistance *R*. $u_{\rm dc}$ is dc voltage, $i_{\rm dc}$ is dc current, and $u_{{\rm ac}j}$ and $i_{{\rm ac}j}$ are ac output voltage and current of phase j ($j \in \{\rm A, B, C\}$), respectively. The voltages and currents of arms are drawn in the figure, where the subscript "u" and "l" denote upper and lower arms, respectively. The equivalent

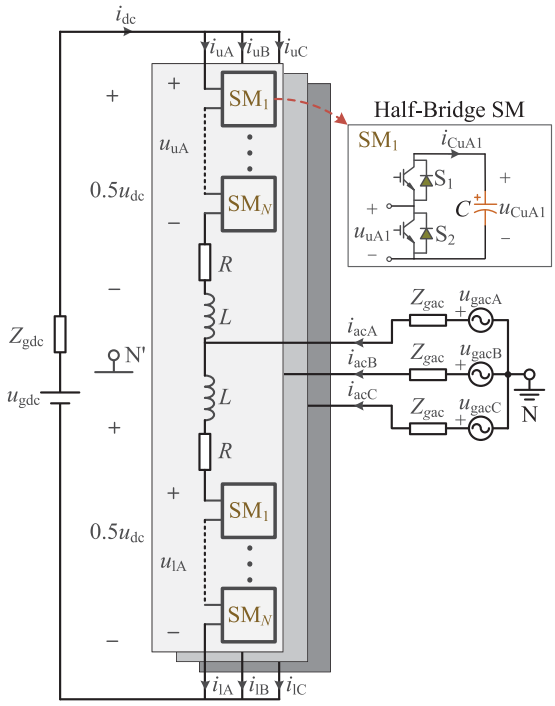

Fig. 1. Circuit configuration of MMC.

impedances of ac and dc grids are expressed as $Z_{\rm gac}$ and $Z_{\rm gdc}$, respectively, whereas the grid sources are denoted as $u_{\rm gdc}$ and $u_{{\rm gac}j}$. For simplification, an ideal balancing between SMs in one arm is assumed since the influence of the SMs differences on the MMC impedance is negligible [21]–[23]. Applying the *Kirchhoff Voltage Law* to the circuit, the MMC three-phase model can be obtained as

$$u_{\rm gdc} = u_{{\rm l}j} + u_{{\rm u}j} + R\left(i_{{\rm l}j} + i_{{\rm u}j}\right) + L\frac{d\left(i_{{\rm l}j} + i_{{\rm u}j}\right)}{dt} + u_{Z{\rm gdc}} \tag{1a}$$

$$u_{{\rm gac}j} = \frac{u_{{\rm l}j} - u_{{\rm u}j}}{2} + \frac{R}{2}\left(i_{{\rm l}j} - i_{{\rm u}j}\right) + \frac{L}{2}\frac{d\left(i_{{\rm l}j} - i_{{\rm u}j}\right)}{dt} + u_{Z{\rm gac}j} + u_{\rm N'N} \tag{1b}$$

$$i_{{\rm Cu}j} = C\frac{du_{{\rm Cu}j}}{dt}, \quad i_{{\rm Cl}j} = C\frac{du_{{\rm Cl}j}}{dt} \tag{1c}$$

where

$$Ni_{{\rm Cu}j} = i_{{\rm u}j}Nm_{{\rm u}j}, \quad Ni_{{\rm Cl}j} = i_{{\rm l}j}Nm_{{\rm l}j} \tag{2a}$$

$$u_{{\rm u}j} = u_{{\rm Cu}j}Nm_{{\rm u}j}, \quad u_{{\rm l}j} = u_{{\rm Cl}j}Nm_{{\rm l}j} \tag{2b}$$

$$i_{\rm dc} = \sum_{j=\{\rm A,B,C\}} i_{{\rm u}j} = \sum_{j=\{\rm A,B,C\}} i_{{\rm l}j} \tag{2c}$$

$$u_{\rm N'N} = -\frac{1}{3}\left(\frac{u_{\rm lA} - u_{\rm uA}}{2} + \frac{u_{\rm lB} - u_{\rm uB}}{2} + \frac{u_{\rm lC} - u_{\rm uC}}{2}\right). \tag{2d}$$

where $u_{{\rm Cu}j}$ and $u_{{\rm Cl}j}$ represent the average SM capacitor voltages of upper and lower arms, respectively.m denotes the modulation index that has the range from zero (all SMs bypassed) to one (all SMs inserted). $u_{\rm N'N}$ denotes the ZS voltage between neutral point N' (in dc side) and N (in ac grid side). $u_{Z{\rm gdc}}$ and $u_{Z{\rm gac}j}$ are voltages across the dc and ac grid impedances, respectively, that is

$$\begin{cases} u_{Z{\rm gdc}} = \mathscr{F}^{-1}\left[Z_{\rm gdc}\left(\omega\right) i_{\rm dc}\left(\omega\right)\right] \\ u_{Z{\rm gac}j} = \mathscr{F}^{-1}\left[Z_{\rm gac}\left(\omega\right) i_{{\rm ac}j}\left(\omega\right)\right]. \end{cases} \tag{3}$$

Note that these voltages are expressed by inverse Fourier transformation since the impedance belongs to frequency domain. This inverse Fourier transformation will be removed during the HSS modeling procedure, and thus it will not introduce extra complexity into the final impedance model.

It is observed from (1) that the ac and dc sides of MMC are affected by the sum and the difference of upper and lower arm variables, respectively. Therefore, the model can be simplified with the concept of differential mode (DM) and common mode (CM) [35] by expressing an arbitrary variable x in (1) and (2) as

$$\begin{cases} x_{{\rm dm}j} = \left(x_{{\rm l}j} - x_{{\rm u}j}\right)/2 \\ x_{{\rm cm}j} = \left(x_{{\rm l}j} + x_{{\rm u}j}\right)/2. \end{cases} \tag{4}$$

Then, the MMC three-phase model becomes

$$\begin{cases} u_{\rm gdc} = 2u_{{\rm cm}j} + 2Ri_{{\rm cm}j} + 2L\frac{di_{{\rm cm}j}}{dt} + \mathscr{F}^{-1}\left[Z_{\rm gdc}\left(\omega\right) i_{\rm dc}\left(\omega\right)\right] \\ u_{{\rm gac}j} = u_{{\rm dm}j} + \frac{R}{2}i_{{\rm ac}j} + \frac{L}{2}\frac{di_{{\rm ac}j}}{dt} + \mathscr{F}^{-1}\left[Z_{\rm gac}\left(\omega\right) i_{{\rm ac}j}\left(\omega\right)\right] + u_{\rm N'N} \\ C\frac{du_{{\rm Ccm}j}}{dt} = m_{{\rm cm}j}i_{{\rm cm}j} + \frac{1}{2}m_{{\rm dm}j}i_{{\rm ac}j} \\ C\frac{du_{{\rm Cdm}j}}{dt} = \frac{1}{2}m_{{\rm cm}j}i_{{\rm ac}j} + m_{{\rm dm}j}i_{{\rm cm}j} \end{cases} \tag{5}$$

where

$$i_{\rm dc} = \sum_{j=\{\rm A,B,C\}} i_{{\rm cm}j}, \quad i_{{\rm ac}j} = 2i_{{\rm dm}j} \tag{6a}$$

$$u_{{\rm cm}j} = N\left(m_{{\rm cm}j}u_{{\rm Ccm}j} + m_{{\rm dm}j}u_{{\rm Cdm}j}\right) \tag{6b}$$

$$u_{{\rm dm}j} = N\left(m_{{\rm cm}j}u_{{\rm Cdm}j} + m_{{\rm dm}j}u_{{\rm Ccm}j}\right) \tag{6c}$$

$$u_{\rm N'N} = -\frac{1}{3}\left(u_{\rm dmA} + u_{\rm dmB} + u_{\rm dmC}\right) \tag{6d}$$

where $m_{{\rm cm}j}$, $m_{{\rm dm}j}$ and $u_{{\rm Ccm}j}$, $u_{{\rm Cdm}j}$ denote the CM/DM components of modulation indexes and SM capacitor voltages, respectively. $i_{{\rm cm}j}$ is the circulating current of MMC. Equation (5) shows that $i_{{\rm cm}j}$ is controlled by adjusting $m_{{\rm cm}j}$, whereas the $i_{{\rm ac}j}$ is controlled by $m_{{\rm dm}j}$. This feature makes the MMC model capable of connecting with the controllers where $m_{{\rm cm}j}$ and $m_{{\rm dm}j}$ come from.

B. Single-Phase Equivalent Model of MMC

In (6), both $i_{\rm dc}$ and $u_{\rm N'N}$ consist of three-phase variables, leading to a complex 12th-order expression. To simplify it and reduce the order, a single-phase equivalent model of MMC is derived in this section.

In MMC, only ZS component of $i_{{\rm cm}j}$ flows into the dc side, whereas the positive- and negative-sequence (PS and NS) components are counteracted. Therefore, $i_{\rm dc}$ can be simplified

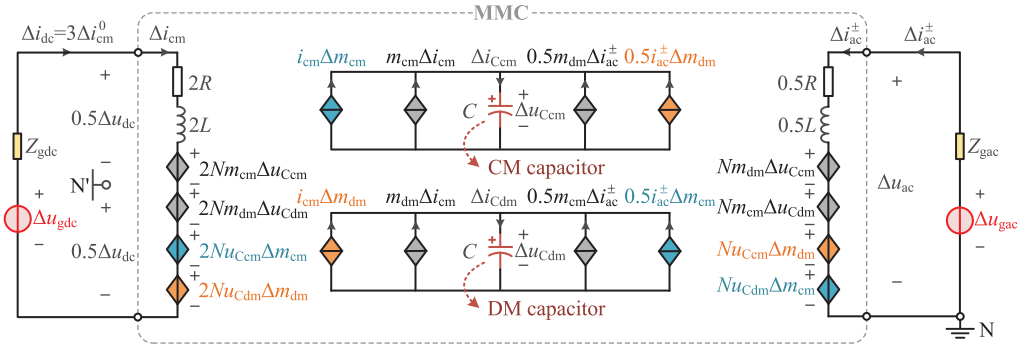

Fig. 2. Equivalent circuit of the MMC linear model in (8), and (9).

as the three times of the $i_{\mathrm{cm}j}$ ZS component. On the other hand, from the ac side, MMC is connected to a three-phase three-wire system where only the PS and NS components appear in $i_{\mathrm{ac}j}$ and the ZS voltage $u_{\mathrm{N'N}}$ cannot cause any ZS current [26]. Thus, the influence of $u_{\mathrm{N'N}}$ on MMC can be reflected by removing the ZS component from $i_{\mathrm{ac}j}$. Rewriting (5), we have

$$\begin{cases} u_{\mathrm{gdc}} = 2u_{\mathrm{cm}} + 2Ri_{\mathrm{cm}} + 2L\frac{di_{\mathrm{cm}}}{dt} \\ \qquad\quad + \mathscr{F}^{-1}\left[Z_{\mathrm{gdc}}(\omega)\, 3i^{0}_{\mathrm{cm}}(\omega)\right] \\ u_{\mathrm{gac}} = u_{\mathrm{dm}} + \frac{R}{2}i^{\pm}_{\mathrm{ac}} + \frac{L}{2}\frac{di^{\pm}_{\mathrm{ac}}}{dt} + \mathscr{F}^{-1}\left[Z_{\mathrm{gac}}(\omega)\, i^{\pm}_{\mathrm{ac}}(\omega)\right] \\ C\frac{du_{\mathrm{Ccm}}}{dt} = m_{\mathrm{cm}}i_{\mathrm{cm}} + \frac{1}{2}m_{\mathrm{dm}}i^{\pm}_{\mathrm{ac}} \\ C\frac{du_{\mathrm{Cdm}}}{dt} = \frac{1}{2}m_{\mathrm{cm}}i^{\pm}_{\mathrm{ac}} + m_{\mathrm{dm}}i_{\mathrm{cm}}. \end{cases} \tag{7}$$

Note that the superscript "0" and "±" indicate ZS and PS/NS components, respectively, by which i_{dc} preserves the ZS component (i.e., $3i^{0}_{\mathrm{cm}}$), whereas i_{ac} removes it (i.e., $i^{\pm}_{\mathrm{ac}}$). As a result, all three-phase variables are expressed in a single-phase form, obtaining a single-phase equivalent model of MMC.

III. MMC Open-Loop Impedance Model Based on HSS and Grid Impedance Coupling

A. Linear Time-Invariant MMC Model

The impedance model is essentially a time-invariant linear model, and therefore (7) needs to be linearized first and then transformed into a time-invariant model.

For linearization, applying the small-signal method to (7), we have

$$\begin{cases} \Delta u_{\mathrm{gdc}} = 2\Delta u_{\mathrm{cm}} + 2R\Delta i_{\mathrm{cm}} + 2L\frac{d\Delta i_{\mathrm{cm}}}{dt} \\ \qquad\quad + \mathscr{F}^{-1}\left[Z_{\mathrm{gdc}}(\omega)\, 3\Delta i^{0}_{\mathrm{cm}}(\omega)\right] \\ \Delta u_{\mathrm{gac}} = \Delta u_{\mathrm{dm}} + \frac{R}{2}\Delta i^{\pm}_{\mathrm{ac}} + \frac{L}{2}\frac{d\Delta i^{\pm}_{\mathrm{ac}}}{dt} \\ \qquad\quad + \mathscr{F}^{-1}\left[Z_{\mathrm{gac}}(\omega)\, \Delta i^{\pm}_{\mathrm{ac}}(\omega)\right] \\ C\frac{d\Delta u_{\mathrm{Ccm}}}{dt} = m_{\mathrm{cm}}\Delta i_{\mathrm{cm}} + i_{\mathrm{cm}}\Delta m_{\mathrm{cm}} + \frac{1}{2}m_{\mathrm{dm}}\Delta i^{\pm}_{\mathrm{ac}} \\ \qquad\quad + \frac{1}{2}i^{\pm}_{\mathrm{ac}}\Delta m_{\mathrm{dm}} \\ C\frac{d\Delta u_{\mathrm{Cdm}}}{dt} = \frac{1}{2}m_{\mathrm{cm}}\Delta i^{\pm}_{\mathrm{ac}} + \frac{1}{2}i^{\pm}_{\mathrm{ac}}\Delta m_{\mathrm{cm}} + m_{\mathrm{dm}}\Delta i_{\mathrm{cm}} \\ \qquad\quad + i_{\mathrm{cm}}\Delta m_{\mathrm{dm}} \end{cases} \tag{8}$$

where

$$\begin{cases} \Delta u_{\mathrm{cm}} = N\left(m_{\mathrm{cm}}\Delta u_{\mathrm{Ccm}} + u_{\mathrm{Ccm}}\Delta m_{\mathrm{cm}}\right. \\ \qquad\quad \left. + m_{\mathrm{dm}}\Delta u_{\mathrm{Cdm}} + u_{\mathrm{Cdm}}\Delta m_{\mathrm{dm}}\right) \\ \Delta u_{\mathrm{dm}} = N\left(m_{\mathrm{cm}}\Delta u_{\mathrm{Cdm}} + u_{\mathrm{Cdm}}\Delta m_{\mathrm{cm}}\right. \\ \qquad\quad \left. + m_{\mathrm{dm}}\Delta u_{\mathrm{Ccm}} + u_{\mathrm{Ccm}}\Delta m_{\mathrm{dm}}\right). \end{cases} \tag{9}$$

The symbol Δ denotes small-signal component, and the variables without Δ represent the steady-state operating point. Equivalent circuit of the MMC linear model (8) and (9) is presented in Fig. 2, where the SM capacitors are decomposed into DM and CM parts. The dependent sources colored in gray relate to the transmission path of the state variables perturbation, whereas that in orange and blue characterize the influence caused by DM and CM modulation indexes perturbation (Δm_{cm}, Δm_{dm}), respectively.

When MMC operates normally, all variables in (8) and (9) would be periodically time-varying so they need to be transferred to time-invariant expressions using the HSS theory [15]–[17]. In HSS, variables are transformed from time domain into the frequency domain, presented by Fourier coefficients as

$$x(t) = \sum_{n\in Z} x_n e^{jn\omega_1 t} \tag{10}$$

where $x(t)$ is an arbitrary steady variable in (8) and (9); ω_1 is the fundamental angular frequency; n denotes the harmonic order; and x_n is Fourier coefficient of the nth harmonic, a complex number containing the signal amplitude and initial phase angle. Likewise, the perturbation in $x(t)$, that is $\Delta x(t)$, satisfies

$$\Delta x(t) = \sum_{n\in Z} x_{p+n} e^{j(p+n)\omega_1 t} \tag{11}$$

in which $p = \omega_p/\omega_1$; ω_p denotes perturbation frequency; and x_{p+n} is relative to the frequency of $\omega_p + n\omega_1$. The multiplication of $\Delta x(t)$ and its steady-state coefficient $a(t)$ in HSS is expressed by the discrete convolution as

$$a(t)\,\Delta x(t) = \sum_{n,m\in Z} a_{n-m} x_{p+m} e^{j(p+n)\omega_1 t} \tag{12}$$

which can be rewritten as the matrix form, such as

$$a(t)\Delta x(t) \Rightarrow \mathbf{A}\Delta\mathbf{x} = \begin{bmatrix} \ddots & \vdots & \vdots & \vdots & \iddots \\ \cdots & a_0 & a_{-1} & a_{-2} & \cdots \\ \cdots & a_1 & a_0 & a_{-1} & \cdots \\ \cdots & a_2 & a_1 & a_0 & \cdots \\ \iddots & \vdots & \vdots & \vdots & \ddots \end{bmatrix} \begin{bmatrix} \vdots \\ x_{p-1} \\ x_p \\ x_{p+1} \\ \vdots \end{bmatrix}. \quad (13)$$

A is called the Toeplitz matrix, and the subscripts of the matrix elements indicate the harmonics order. For the derivative of $\Delta x(t)$, it is given by

$$\Delta\dot{x}(t) = \sum_{n\in Z} j(p+n)\omega_1 x_{p+n} e^{j(p+n)\omega_1 t} \quad (14)$$

which can also be written as the following matrix:

$$\Delta\dot{x}(t) \Rightarrow \Delta\mathbf{S}\Delta\mathbf{x} = \begin{bmatrix} \ddots & & & & & \\ & j(p-1)\omega_1 & & & & \\ & & jp\omega_1 & & & \\ & & & j(p+1)\omega_1 & & \\ & & & & \ddots \end{bmatrix} \begin{bmatrix} \vdots \\ x_{p-1} \\ x_p \\ x_{p+1} \\ \vdots \end{bmatrix} \quad (15)$$

where $\Delta\mathbf{S}$ is the coefficient matrix of the derivative in HSS, which contains all frequency information of $\Delta x(t)$.

According to (10)–(15), the time-varying MMC model (8) and (9) will be transformed into HSS, that is

$$\begin{cases} \Delta\mathbf{u}_{\rm gdc} = 2\Delta\mathbf{u}_{\rm cm} + 2R\Delta\mathbf{i}_{\rm cm} + 2L\Delta\mathbf{S}\Delta\mathbf{i}_{\rm cm} + 3\mathbf{Z}_{\rm gdc}\Delta\mathbf{i}^0_{\rm cm} \\ \Delta\mathbf{u}_{\rm gac} = \Delta\mathbf{u}_{\rm dm} + \frac{R}{2}\Delta\mathbf{i}^{\pm}_{\rm ac} + \frac{L}{2}\Delta\mathbf{S}\Delta\mathbf{i}^{\pm}_{\rm ac} + \mathbf{Z}_{\rm gac}\Delta\mathbf{i}^{\pm}_{\rm ac} \\ C\Delta\mathbf{S}\Delta\mathbf{u}_{\rm Ccm} = \mathbf{m}_{\rm cm}\Delta\mathbf{i}_{\rm cm} + \mathbf{i}_{\rm cm}\Delta\mathbf{m}_{\rm cm} + \frac{1}{2}\mathbf{m}_{\rm dm}\Delta\mathbf{i}^{\pm}_{\rm ac} \\ \qquad\qquad + \frac{1}{2}\mathbf{i}^{\pm}_{\rm ac}\Delta\mathbf{m}_{\rm dm} \\ C\Delta\mathbf{S}\Delta\mathbf{u}_{\rm Cdm} = \frac{1}{2}\mathbf{m}_{\rm cm}\Delta\mathbf{i}^{\pm}_{\rm ac} + \frac{1}{2}\mathbf{i}^{\pm}_{\rm ac}\Delta\mathbf{m}_{\rm cm} + \mathbf{m}_{\rm dm}\Delta\mathbf{i}_{\rm cm} \\ \qquad\qquad + \mathbf{i}_{\rm cm}\Delta\mathbf{m}_{\rm dm} \end{cases} \quad (16)$$

where

$$\begin{cases} \Delta\mathbf{u}_{\rm cm} = N(\mathbf{m}_{\rm cm}\Delta\mathbf{u}_{\rm Ccm} + \mathbf{u}_{\rm Ccm}\Delta\mathbf{m}_{\rm cm} + \mathbf{m}_{\rm dm}\Delta\mathbf{u}_{\rm Cdm} \\ \qquad\qquad + \mathbf{u}_{\rm Cdm}\Delta\mathbf{m}_{\rm dm}) \\ \Delta\mathbf{u}_{\rm dm} = N(\mathbf{m}_{\rm cm}\Delta\mathbf{u}_{\rm Cdm} + \mathbf{u}_{\rm Cdm}\Delta\mathbf{m}_{\rm cm} + \mathbf{m}_{\rm dm}\Delta\mathbf{u}_{\rm Ccm} \\ \qquad\qquad + \mathbf{u}_{\rm Ccm}\Delta\mathbf{m}_{\rm dm}) \end{cases} \quad (17a)$$

$$\mathbf{Z}_{\rm gdc/ac} = {\rm diag}\left[\ldots, Z_{\rm gdc/ac}(\omega_{p-2}), Z_{\rm gdc/ac}(\omega_{p-1}), Z_{\rm gdc/ac}(\omega_p), Z_{\rm gdc/ac}(\omega_{p+1}), Z_{\rm gdc/ac}(\omega_{p+2}), \ldots\right]. \quad (17b)$$

All variables are represented by time-invariant matrixes or vectors containing MMC internal harmonics, by which the linear time-invariant MMC model is obtained.

B. Sequence Analysis of MMC Small-Signal Response

It can be found that the variables in the model (16) are nonuniform due to the different sequence components involved. For instance, both $\Delta\mathbf{i}_{\rm cm}$ and $\Delta\mathbf{i}^0_{\rm cm}$ belong to the circulating current, but they cannot be directly incorporated. This problem makes it difficult to simplify (16) to derive the MMC impedance. Therefore, this section aims to clearly analyze the MMC sequence feature under perturbations and then utilize it to unify the expressions of different sequences to further facilitate the MMC impedance derivation.

In the steady state, the arbitrary three-phase MMC variables can be written as

$$\begin{cases} x_{\rm A}(t) = \sum_{n\in Z} x_n e^{jn\omega_1 t} \\ x_{\rm B}(t) = \sum_{n\in Z} x_n e^{j(n\omega_1 t - n120^\circ)} \\ x_{\rm C}(t) = \sum_{n\in Z} x_n e^{j(n\omega_1 t + n120^\circ)} \end{cases} \quad (18)$$

where the ZS component appears if the harmonics order n equals an integer multiple of 3 (i.e., $n = 3k$, k belongs to an integer), whereas the PS and NS components are corresponding to $n = 3k+1$ and $n = 3k-1$, respectively. This principle, however, is no longer valid for MMC small-signal responses since the perturbation injected into the MMC will interact with the steady-state component, changing the sequence of the responses.

When the three-phase PS perturbation is injected into the MMC ac side, the small-signal response will be generated as

$$\begin{cases} \Delta x_{\rm A}(t) = \sum_{n\in Z} x_{p+n} e^{j(p+n)\omega_1 t} \\ \Delta x_{\rm B}(t) = \sum_{n\in Z} x_{p+n} e^{j[(p+n)\omega_1 t - (n+1)120^\circ]} \\ \Delta x_{\rm C}(t) = \sum_{n\in Z} x_{p+n} e^{j[(p+n)\omega_1 t + (n+1)120^\circ]}. \end{cases} \quad (19)$$

It can be seen that (19) contains phase angles of both the steady-state variables and the perturbations. This causes the sequence of the response affected by $(n+1)$ instead of n. Note that the sequence in this article is determined based on initial phases. If the initial phases of the signals in phases A, B, and C are lagging by 120°, they belong to PS components, otherwise they are NS components. Under this definition, for example, even if $p+n<0$ in (19), the signals can still be regarded as a PS components with a negative frequency when $(n+1) = 3k+1$.

Likewise, the ac NS perturbation leads to

$$\begin{cases} \Delta x_{\rm A}(t) = \sum_{n\in Z} x_{p+n} e^{j(p+n)\omega_1 t} \\ \Delta x_{\rm B}(t) = \sum_{n\in Z} x_{p+n} e^{j[(p+n)\omega_1 t - (n-1)120^\circ]} \\ \Delta x_{\rm C}(t) = \sum_{n\in Z} x_{p+n} e^{j[(p+n)\omega_1 t + (n-1)120^\circ]} \end{cases} \quad (20)$$

where the sequence is determined by $(n-1)$.

Moreover, if the perturbation is injected from the dc side, since the perturbation is identical for each phase of the MMC (which is equivalent to inject ZS perturbation), the response will

still remain the sequence of the steady state

$$\begin{cases} \Delta x_{\mathrm{A}}(t) = \sum_{n\in Z} x_{p+n} e^{j(p+n)\omega_1 t} \\ \Delta x_{\mathrm{B}}(t) = \sum_{n\in Z} x_{p+n} e^{j[(p+n)\omega_1 t - n120^\circ]} \\ \Delta x_{\mathrm{C}}(t) = \sum_{n\in Z} x_{p+n} e^{j[(p+n)\omega_1 t + n120^\circ]}. \end{cases} \tag{21}$$

Obviously, when the perturbations with different sequences are injected from the MMC ac or dc side, the sequence of the small-signal responses is completely different. It depends not only on the order of the harmonics but also on the position of the injected perturbation.

In addition to the sequence, the harmonic frequency in the MMC small-signal response is also different when perturbations are injected from the ac and dc sides. As shown in Fig. 2, a three-phase perturbation (PS or NS) with frequency ω_p injected from MMC ac side causes a same frequency response in $\Delta i_{\mathrm{ac}}^{\pm}$. This current will generate harmonics with frequency $\omega_p \pm \omega_1$ into the CM capacitor voltage Δu_{Ccm} as $0.5 m_{\mathrm{dm}} \Delta i_{\mathrm{ac}}^{\pm}$ is the product of two frequency components. And these harmonics in Δu_{Ccm} are introduced into the circulating current Δi_{cm} by the dependent source $2N m_{\mathrm{cm}} \Delta u_{\mathrm{Ccm}}$. Likewise, the harmonics in Δi_{cm} further affects the DM capacitor voltage Δu_{Cdm} through the current source $m_{\mathrm{dm}} \Delta i_{\mathrm{cm}}$, leading to harmonics at ω_p and $\omega_p \pm 2\omega_1$. Eventually, infinite components in CM variables, such as Δu_{Ccm}, Δm_{cm}, and Δi_{cm}, are coupled with the odd multiple of ω_1, whereas that in DM variables, such as Δu_{Cdm}, Δi_{ac}, and Δm_{dm}, are coupled with the even multiple of ω_1. Conversely, if the perturbation is injected from the MMC dc side, under the influence of dependent sources $m_{\mathrm{cm}} \Delta i_{\mathrm{cm}}$ and $m_{\mathrm{dm}} \Delta i_{\mathrm{cm}}$, the current response Δi_{cm} will lead infinite harmonics to Δu_{Ccm} and Δu_{Cdm}, with frequency $\omega_p \pm 2k\omega_1$ and $\omega_p \pm (2k+1)\omega_1$, respectively. It can be found that the frequency components in CM and DM variables are different from the case injecting voltage at MMC ac side.

Aforementioned discussions is summarized in Table I, which shows the relationship between the sequence and the frequency for arbitrary MMC variables. The table also reflects the harmonic frequencies of the CM and DM variables with different perturbations. Table I(a) lists the frequency under the steady state, which conforms to the description of (18). After injecting the perturbation, the perturbation frequency interacts with the steady-state components and changes the sequence of the responses, as shown in Table I(b)–(d).

In order to unify expressions of different sequences, the following sequence extraction matrixes are introduced to extract the certain sequence from HSS variables:

$$\begin{cases} \mathbf{E}_{-}^{+} = \mathrm{diag}(\ldots, 0, 1, 0, 0, 1, 0, 0, \ldots) \\ \mathbf{E}_{0}^{+} = \mathrm{diag}(\ldots, 0, 0, 1, 0, 0, 1, 0, \ldots) \\ \mathbf{E}_{+}^{+} = \mathrm{diag}(\ldots, 1, 0, 0, 1, 0, 0, 1, \ldots) \end{cases} \tag{22a}$$

$$\begin{cases} \mathbf{E}_{-}^{-} = \mathrm{diag}(\ldots, 1, 0, 0, 1, 0, 0, 1, \ldots) \\ \mathbf{E}_{0}^{-} = \mathrm{diag}(\ldots, 0, 1, 0, 0, 1, 0, 0, \ldots) \\ \mathbf{E}_{+}^{-} = \mathrm{diag}(\ldots, 0, 0, 1, 0, 0, 1, 0, \ldots) \end{cases} \tag{22b}$$

TABLE I
RELATIONSHIP BETWEEN THE SEQUENCE AND THE FREQUENCY FOR ARBITRARY MMC VARIABLES UNDER DIFFERENT PERTURBATIONS

Sequence	frequency				
	(a) Steady-state				
NS	$-7\omega_1$ (DM)	$-4\omega_1$ (CM)	$-\omega_1$ (DM)	$2\omega_1$ (CM)	$5\omega_1$ (DM)
ZS	$-6\omega_1$ (CM)	$-3\omega_1$ (DM)	0 (CM)	$3\omega_1$ (DM)	$6\omega_1$ (CM)
PS	$-5\omega_1$ (DM)	$-2\omega_1$ (CM)	ω_1 (DM)	$4\omega_1$ (CM)	$7\omega_1$ (DM)
	(b) Inject PS perturbation from ac side				
ZS	ω_p−$7\omega_1$ (CM)	ω_p−$4\omega_1$ (DM)	ω_p−ω_1 (CM)	ω_p+$2\omega_1$ (DM)	ω_p+$5\omega_1$ (CM)
PS	ω_p−$6\omega_1$ (DM)	ω_p−$3\omega_1$ (CM)	ω_p (DM)	ω_p+$3\omega_1$ (CM)	ω_p+$6\omega_1$ (DM)
NS	ω_p−$5\omega_1$ (CM)	ω_p−$2\omega_1$ (DM)	ω_p+ω_1 (CM)	ω_p+$4\omega_1$ (DM)	ω_p+$7\omega_1$ (CM)
	(c) Inject NS perturbation from ac side				
PS	ω_p−$7\omega_1$ (CM)	ω_p−$4\omega_1$ (DM)	ω_p−ω_1 (CM)	ω_p+$2\omega_1$ (DM)	ω_p+$5\omega_1$ (CM)
NS	ω_p−$6\omega_1$ (DM)	ω_p−$3\omega_1$ (CM)	ω_p (DM)	ω_p+$3\omega_1$ (CM)	ω_p+$6\omega_1$ (DM)
ZS	ω_p−$5\omega_1$ (CM)	ω_p−$2\omega_1$ (DM)	ω_p+ω_1 (CM)	ω_p+$4\omega_1$ (DM)	ω_p+$7\omega_1$ (CM)
	(d) Inject perturbation from dc side				
NS	ω_p−$7\omega_1$ (DM)	ω_p−$4\omega_1$ (CM)	ω_p−ω_1 (DM)	ω_p+$2\omega_1$ (CM)	ω_p+$5\omega_1$ (DM)
ZS	ω_p−$6\omega_1$ (CM)	ω_p−$3\omega_1$ (DM)	ω_p (CM)	ω_p+$3\omega_1$ (DM)	ω_p+$6\omega_1$ (CM)
PS	ω_p−$5\omega_1$ (DM)	ω_p−$2\omega_1$ (CM)	ω_p+ω_1 (DM)	ω_p+$4\omega_1$ (CM)	ω_p+$7\omega_1$ (DM)

$$\begin{cases} \mathbf{E}_{-}^{0} = \mathrm{diag}(\ldots, 0, 0, 1, 0, 0, 1, 0, \ldots) \\ \mathbf{E}_{0}^{0} = \mathrm{diag}(\ldots, 1, 0, 0, 1, 0, 0, 1, \ldots) \\ \mathbf{E}_{+}^{0} = \mathrm{diag}(\ldots, 0, 1, 0, 0, 1, 0, 0, \ldots) \end{cases} \tag{22c}$$

in which the superscript indicates the sequence of the injected perturbation, whereas the subscript indicates the sequence to be extracted. For example, the matrix $\mathbf{E}_{-}^{+}$ can extract the NS component after the PS perturbation is injected from the ac side, and $\mathbf{E}_{+}^{0}$ is used to extract the PS component when the perturbation is injected from the dc side.

Applying (22), the ac current and the circulating current can be unified as

$$\Delta \mathbf{i}_{\mathrm{cm}}^{0} = \mathbf{E}_{0}^{s} \Delta \mathbf{i}_{\mathrm{cm}} \tag{23a}$$

$$\Delta \mathbf{i}_{\mathrm{ac}}^{\pm} = \left(\mathbf{E}_{+}^{s} + \mathbf{E}_{-}^{s}\right) \Delta \mathbf{i}_{\mathrm{ac}} = \mathbf{E}_{\pm}^{s} \Delta \mathbf{i}_{\mathrm{ac}} \tag{23b}$$

where $s \in \{+, -, 0\}$ denote the PS, NS, and ZS, respectively. With (23), the linear time-invariant MMC model (16) can be simplified to

$$\underbrace{\begin{bmatrix} \Delta \mathbf{u}_{\mathrm{gdc}} \\ \Delta \mathbf{u}_{\mathrm{gac}} \end{bmatrix}}_{\Delta \mathbf{u}_{\mathrm{g}}} = \underbrace{\left(\begin{bmatrix} \mathbf{K}_{i\mathrm{cm}1} & \mathbf{K}_{i1} \\ \mathbf{K}_{i\mathrm{cm}2} & \mathbf{K}_{i2} \end{bmatrix} + \begin{bmatrix} 3\mathbf{Z}_{\mathrm{gdc}} \mathbf{E}_{0}^{s} & \\ & \mathbf{Z}_{\mathrm{gac}} \mathbf{E}_{\pm}^{s} \end{bmatrix} \right)}_{(\mathbf{K}_i + \mathbf{Z}_{\mathrm{g}})} \times \underbrace{\begin{bmatrix} \Delta \mathbf{i}_{\mathrm{cm}} \\ \Delta \mathbf{i}_{\mathrm{ac}} \end{bmatrix}}_{\Delta \mathbf{i}} + \underbrace{\begin{bmatrix} \mathbf{K}_{m\mathrm{cm}1} & \mathbf{K}_{m\mathrm{dm}1} \\ \mathbf{K}_{m\mathrm{cm}2} & \mathbf{K}_{m\mathrm{dm}2} \end{bmatrix}}_{\mathbf{K}_m} \underbrace{\begin{bmatrix} \Delta \mathbf{m}_{\mathrm{cm}} \\ \Delta \mathbf{m}_{\mathrm{dm}} \end{bmatrix}}_{\Delta \mathbf{m}} \tag{24a}$$

$$\begin{cases} \mathbf{K}_{icm1} = 2R\mathbf{I} + 2L\Delta\mathbf{S} + \frac{2N}{C}\mathbf{m}_{cm}\Delta\mathbf{S}^{-1}\mathbf{m}_{cm} \\ \qquad + \frac{2N}{C}\mathbf{m}_{dm}\Delta\mathbf{S}^{-1}\mathbf{m}_{dm} \\ \mathbf{K}_{i1} = \left(\frac{N}{C}\mathbf{m}_{cm}\Delta\mathbf{S}^{-1}\mathbf{m}_{dm} + \frac{N}{C}\mathbf{m}_{dm}\Delta\mathbf{S}^{-1}\mathbf{m}_{cm}\right)\mathbf{E}_{\pm}^{s} \\ \mathbf{K}_{icm2} = \frac{N}{C}\mathbf{m}_{dm}\Delta\mathbf{S}^{-1}\mathbf{m}_{cm} + \frac{N}{C}\mathbf{m}_{cm}\Delta\mathbf{S}^{-1}\mathbf{m}_{dm} \\ \mathbf{K}_{i2} = \left(\frac{R}{2}\mathbf{I} + \frac{L}{2}\Delta\mathbf{S} + \frac{N}{2C}\mathbf{m}_{dm}\Delta\mathbf{S}^{-1}\mathbf{m}_{dm}\right. \\ \qquad \left. + \frac{N}{2C}\mathbf{m}_{cm}\Delta\mathbf{S}^{-1}\mathbf{m}_{cm}\right)\mathbf{E}_{\pm}^{s} \end{cases} \tag{24b}$$

$$\begin{cases} \mathbf{K}_{mcm1} = \frac{2N}{C}\mathbf{m}_{cm}\Delta\mathbf{S}^{-1}\mathbf{i}_{cm} + \frac{N}{C}\mathbf{m}_{dm}\Delta\mathbf{S}^{-1}\mathbf{i}_{ac}^{\pm} \\ \qquad + 2N\mathbf{u}_{Ccm} \\ \mathbf{K}_{mdm1} = \frac{N}{C}\mathbf{m}_{cm}\Delta\mathbf{S}^{-1}\mathbf{i}_{ac}^{\pm} + \frac{2N}{C}\mathbf{m}_{dm}\Delta\mathbf{S}^{-1}\mathbf{i}_{cm} \\ \qquad + 2N\mathbf{u}_{Cdm} \\ \mathbf{K}_{mcm2} = \frac{N}{C}\mathbf{m}_{dm}\Delta\mathbf{S}^{-1}\mathbf{i}_{cm} + \frac{N}{2C}\mathbf{m}_{cm}\Delta\mathbf{S}^{-1}\mathbf{i}_{ac}^{\pm} + N\mathbf{u}_{Cdm} \\ \mathbf{K}_{mdm2} = \frac{N}{2C}\mathbf{m}_{dm}\Delta\mathbf{S}^{-1}\mathbf{i}_{ac}^{\pm} + \frac{N}{C}\mathbf{m}_{cm}\Delta\mathbf{S}^{-1}\mathbf{i}_{cm} + N\mathbf{u}_{Ccm} \end{cases} \tag{24c}$$

where $\mathbf{K}_i$ and $\mathbf{K}_m$ are coefficient block matrixes corresponding to the current vector $\Delta\mathbf{i}$ and modulation index vector $\Delta\mathbf{m}$, respectively. $\mathbf{I}$ in (24b) is the unit matrix. This model has a clear physical meaning. It can be seen that the arm inductance L and the parasitic resistance R only appears in $\mathbf{K}_i$, which together with the grid impedance matrix $\mathbf{Z}_g$ weakens the current perturbation $\Delta\mathbf{i}$. $\mathbf{K}_m$ consists of all steady-state variables, such as $\mathbf{i}_{cm}$, $\mathbf{i}_{ac}^{\pm}$, $\mathbf{u}_{Ccm}$, and $\mathbf{u}_{Cdm}$, which will be introduced into the MMC by $\Delta\mathbf{m}$ generated from controllers.

C. Grid Impedance Coupling on MMC

When MMC operates under the open-loop condition, $\Delta\mathbf{m}$ equals zero, which means that the open-loop model is not affected by steady-state variables, such as $\mathbf{i}_{cm}$, $\mathbf{i}_{ac}^{\pm}$, $\mathbf{u}_{Ccm}$, and $\mathbf{u}_{Cdm}$, but only with the passive components (i.e., R, L, and C) of the MMC

$$\Delta\mathbf{u}_g = (\mathbf{K}_i + \mathbf{Z}_g)\,\Delta\mathbf{i}. \tag{25}$$

By setting $\Delta\mathbf{u}_{gdc}$ to 0, the current response at the frequency ω_p, that is $\Delta i_{ac}(\omega_p)$, can be solved by (25) for any given $\Delta u_{gac}(\omega_p)$ in $\Delta\mathbf{u}_g$. Hence, the MMC open-loop ac impedance model is obtained as

$$Z_{ac\_MMC}(\omega_p) = \frac{\Delta u_{gac}(\omega_p)}{\Delta i_{ac}(\omega_p)} - Z_{gac}(\omega_p). \tag{26}$$

Similarly, the open-loop dc impedance model is obtained by setting $\Delta\mathbf{u}_{gac}$ to 0, which gives

$$Z_{dc\_MMC}(\omega_p) = \frac{\Delta u_{gdc}(\omega_p)}{3\Delta i_{cm}(\omega_p)} - Z_{gdc}(\omega_p). \tag{27}$$

Equations (26) and (27) accurately describe the open-loop impedance of the MMC. Note that the $Z_{gac}(\omega_p)$ and $Z_{gdc}(\omega_p)$ are subtracted from (26) and (27), respectively, since the grid impedance does not belong to the MMC, as shown in Fig. 2. However, it does not mean that the grid impedance can be ignored or the grid can be assumed ideal before modeling. Even if the grid impedance is subtracted, it cannot completely eliminate

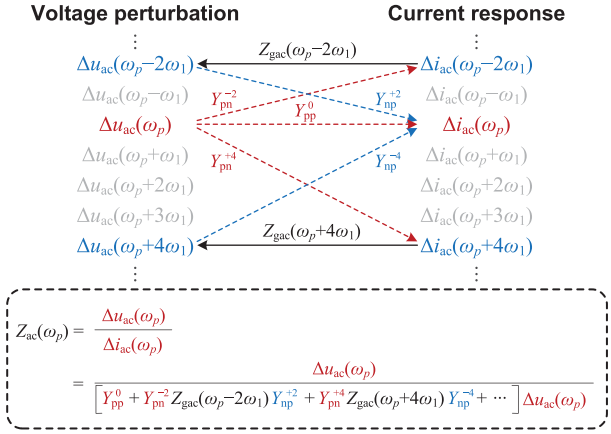

Fig. 3. Schematic diagram of MMC grid impedance coupling (inject PS perturbation voltage at ω_p into ac side).

the impact of the grid impedance on the MMC. This is because the $\mathbf{K}_i$ in (25) is a nondiagonal matrix, by which a perturbation voltage in $\Delta\mathbf{u}_g$ causes MMC to generate a series of harmonic currents into $\Delta\mathbf{i}$. And these currents will flow across the grid impedance, generating new perturbation voltages. Repeatedly like this, the grid impedance values at different perturbation frequencies are introduced into the MMC. Therefore, although the grid impedance at frequency ω_p is subtracted, the information of grid impedance at other frequencies is still presented in the MMC impedance, causing the grid impedance coupling. It shows that the impedance of the MMC itself is not independent, but is affected by the connected grid.

Fig. 3 presents a schematic diagram to explain how the frequency coupling introduces grid impedance into MMC. In this diagram, an ac PS perturbation at ω_p leads to infinite ac current responses, such as $\Delta i_{ac}(\omega_p)$, $\Delta i_{ac}(\omega_p - \omega_2)$, $\Delta i_{ac}(\omega_p + \omega_4)$, etc., where Y_{pp}^{0}, Y_{pn}^{-2}, Y_{np}^{+2}, Y_{pn}^{+4} and Y_{np}^{-4} denote gains of different voltage perturbations to current responses. Besides $\Delta i_{ac}(\omega_p)$, the currents at other frequencies will also flow across the grid impedance, causing voltage drops like $Z_{gac}(\omega_p - \omega_2)\Delta i_{ac}(\omega_p - \omega_2)$ and $Z_{gac}(\omega_p + \omega_4)\Delta i_{ac}(\omega_p + \omega_4)$, etc. These voltages will react on the MMC to generate the current at ω_p and then change ac impedance of MMC. It means that the $\Delta i_{ac}(\omega_p)$ consists of two parts, one part directly generated by the PS perturbation and the other part contributed by the voltage drop of the grid impedance. This makes the MMC impedance affected by the connected grid even if $Z_{gac}(\omega_p)$ is subtracted, which is an important feature of MMC. It can be found from the expression in Fig. 3 that the MMC impedance will decrease as the coupling term increases. Likewise, as listed in Table I(c) and (d), the ac NS perturbation will introduce the grid impedance coupling by producing ac currents at $\omega_p + \omega_2$, $\omega_p - \omega_4$, etc.; the similar coupling also occurs on the MMC dc side, which is caused by dc currents at frequency $\omega_p - \omega_6$, $\omega_p + \omega_6$, etc.

The higher order frequency corresponds to the larger impedance, leading to a smaller current response. Note that the lowest harmonic order in ac current is $\omega_p \pm \omega_2$, whereas in dc

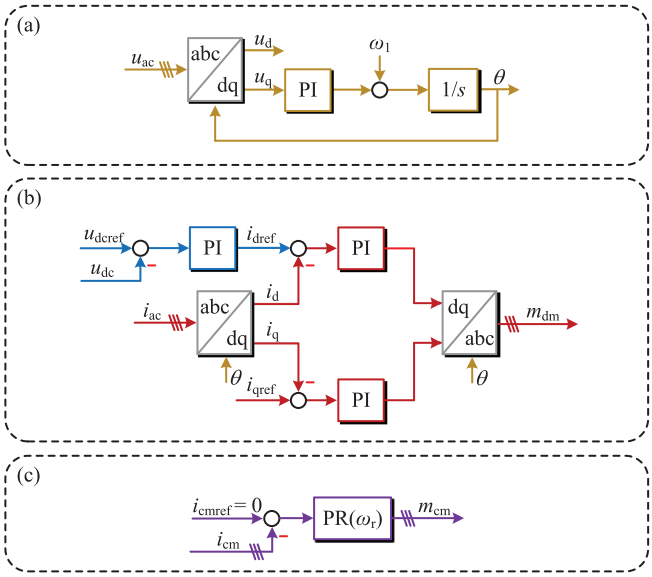

Fig. 4. Control strategies of MMC. (a) PLL. (b) DC voltage–ac current dual loop controller. (c) Circulating current suppression controller.

current is $\omega_p \pm \omega_6$. Therefore, the grid impedance coupling on dc side of the MMC is much weaker than the ac side and can be neglected in practice.

IV. MMC Closed-Loop Impedance Model and the Coupling Caused by the Controllers

Practically, MMC always operates under closed-loop conditions instead of open loop. Fig. 4 shows the commonly used control strategies for MMC, including PLL, ac current inner loop, dc voltage outer loop (dual-loop controllers), and the circulating current suppression. The purpose of this section is to convert these controllers into HSS and connect them with the MMC open-loop model to obtain an MMC closed-loop impedance model.

A. HSS Model of PT and IPT

The PT is the fundamental part of both PLL and ac current controller, which has to be modeled in HSS. Considering the perturbation of the rotation angle, the linearized PT matrix can be written as

$$\begin{aligned} &T_{dq+}\left(\omega_1 t+\Delta\theta\right) \\ &\approx \frac{2}{3}\begin{bmatrix} \cos\omega_1 t & \cos\left(\omega_1 t-120^\circ\right) & \cos\left(\omega_1 t+120^\circ\right) \\ -\sin\omega_1 t & -\sin\left(\omega_1 t-120^\circ\right) & -\sin\left(\omega_1 t+120^\circ\right) \end{bmatrix} \\ &\quad -\frac{2}{3}\begin{bmatrix} \sin\omega_1 t & \sin\left(\omega_1 t-120^\circ\right) & \sin\left(\omega_1 t+120^\circ\right) \\ \cos\omega_1 t & \cos\left(\omega_1 t-120^\circ\right) & \cos\left(\omega_1 t+120^\circ\right) \end{bmatrix}\Delta\theta \\ &= T_{dq+}\left(\omega_1 t\right)+T_{dq+}\left(\omega_1 t+90^\circ\right)\Delta\theta \end{aligned} \tag{28}$$

where $\Delta\theta$ is the perturbation of the rotation angle generated by PLL. Note that the ZS component of PT is removed as it does not exist in the three-phase three-wire system. When PT is applied to a signal with perturbation (i.e., $x+\Delta x$), we have

$$\begin{aligned} &T_{dq+}\left(\omega_1 t+\Delta\theta\right)\left(x+\Delta x\right) \\ &\quad \approx T_{dq+}\left(\omega_1 t\right)\Delta x+T_{dq+}\left(\omega_1 t+90^\circ\right)x\Delta\theta \end{aligned} \tag{29}$$

where the former reflects the effect of the steady-state PT on Δx, and the latter represents the influence of rotation angle perturbation.

As HSS is essentially a model in the frequency domain, (29) needs to be transformed into the frequency domain at first. For the former of (29), that is $T_{dq+}(\omega_1 t)\Delta x$, if Δx is a PS perturbation signal (with the magnitude of Δx), it can be expanded as

$$\begin{aligned} &T_{dq+}\left(\omega_1 t\right)\begin{bmatrix} \Delta X\cos\left(\omega_p t\right) \\ \Delta X\cos\left(\omega_p t-120^\circ\right) \\ \Delta X\cos\left(\omega_p t+120^\circ\right) \end{bmatrix} \\ &= \begin{bmatrix} \Delta X\cos\left[\left(\omega_p-\omega_1\right)t\right] \\ \Delta X\cos\left[\left(\omega_p-\omega_1\right)t-90^\circ\right] \end{bmatrix}. \end{aligned} \tag{30}$$

Equation (30) shows that the PT can reduce the frequency of the signal, and the q-axis component lags behind the d-axis component by 90°.

Similarly, when Δx is an NS signal, it is given as

$$\begin{aligned} &T_{dq+}\left(\omega_1 t\right)\begin{bmatrix} \Delta X\cos\left(\omega_p t\right) \\ \Delta X\cos\left(\omega_p t+120^\circ\right) \\ \Delta X\cos\left(\omega_p t-120^\circ\right) \end{bmatrix} \\ &= \begin{bmatrix} \Delta X\cos\left[\left(\omega_p+\omega_1\right)t\right] \\ \Delta X\cos\left[\left(\omega_p+\omega_1\right)t+90^\circ\right] \end{bmatrix} \end{aligned} \tag{31}$$

where the frequency shift effect is exactly opposite to (30), and the q-axis component leads the d-axis component by 90°.

Cowrite (30) and (31) into frequency domain, that is

$$\begin{bmatrix} \Delta X_d\left(\omega_p\right) \\ \Delta X_q\left(\omega_p\right) \end{bmatrix} = \begin{bmatrix} 1 \\ \mp j \end{bmatrix}\Delta X\left(\omega_p\pm\omega_1\right). \tag{32}$$

It can be seen that the PT has different frequency shift directions according to the perturbation sequences. Therefore, this article introduces a frequency shift matrix to describe this phenomenon. The transformation for the d-axis component in (32) can be written as

$$\begin{aligned} \mathbf{T}_{\mathrm{d}+} &= \begin{bmatrix} \ddots & 1 & & \\ & 0 & 1 & \\ & & 0 & 1 \\ & & & \ddots \end{bmatrix}\mathbf{E}_+^s+\begin{bmatrix} \ddots & & & \\ 1 & 0 & & \\ & 1 & 0 & \\ & & 1 & \ddots \end{bmatrix}\mathbf{E}_-^s \\ &= \mathbf{T}_{\mathrm{dw}}\mathbf{E}_+^s+\mathbf{T}_{\mathrm{up}}\mathbf{E}_-^s \end{aligned} \tag{33}$$

where $\mathbf{T}_{\mathrm{dw}}$ is defined as the frequency downshift matrix that reduces the frequency by ω_1 for any signal through the PT; and $\mathbf{T}_{\mathrm{up}}$ is defined as the frequency upshift matrix, which increases

the frequency by ω_1; $\mathbf{E}_+^s$ and $\mathbf{E}_-^s$ are used to separate the components of different sequences from the signal. Hence, $\mathbf{T}_{d+}$ can simultaneously reflect the frequency shifting effect of PT on different sequences, which makes the model with more concise form. Likewise, the transformation for the q-axis component is

$$\mathbf{T}_{q+} = -j\mathbf{T}_{\mathrm{dw}}\mathbf{E}_+^s + j\mathbf{T}_{\mathrm{up}}\mathbf{E}_-^s. \tag{34}$$

With regard to the latter item in (29), it is the product between the steady-state signal of *d-/q*-axis $T_{dq+}(\omega_1 t + 90^\circ)x$ and the $\Delta\theta$, satisfying the structure shown in (13). Therefore, this item can be directly written into HSS as $\mathbf{x}'_{d+}\Delta\boldsymbol{\theta}$, $\mathbf{x}'_{q+}\Delta\boldsymbol{\theta}$, where $\mathbf{x}'_{d+}$ and $\mathbf{x}'_{q+}$ denote Toeplitz matrixes of d- and q-axis steady-state signal, respectively.

Finally, the relationship between the PT and the signal, given in (29), can be expressed as the HSS form

$$\begin{cases} \Delta\mathbf{x}_d = \mathbf{T}_{d+}\Delta\mathbf{x} + \mathbf{x'}_{d+}\Delta\boldsymbol{\theta} \\ \Delta\mathbf{x}_q = \mathbf{T}_{q+}\Delta\mathbf{x} + \mathbf{x'}_{q+}\Delta\boldsymbol{\theta}. \end{cases} \tag{35}$$

The IPT can also be addressed in the same way, whose time-domain expression is

$$\begin{aligned} &T_{dq-}\left(\omega_1 t + \Delta\theta\right)\left(x_{dq} + \Delta x_{dq}\right) \\ &\quad \approx T_{dq-}\left(\omega_1 t\right)\Delta x_{dq} + T_{dq-}\left(\omega_1 t + 90^\circ\right)x_{dq}\Delta\theta \end{aligned} \tag{36}$$

where the former, $T_{dq-}(\omega_1 t)\Delta x_{dq}$, can be written into the frequency domain as

$$\begin{aligned} \Delta X\left(\omega_p\right) = \frac{1}{2}\big[&\Delta X_d\left(\omega_p - \omega_1\right) + \Delta X_d\left(\omega_p + \omega_1\right) \\ &+ j\Delta X_q\left(\omega_p - \omega_1\right) - j\Delta X_q\left(\omega_p + \omega_1\right)\big] \end{aligned} \tag{37}$$

and the HSS model of IPT is

$$\begin{cases} \mathbf{T}_{d-} = \frac{1}{2}\mathbf{T}_{\mathrm{dw}} + \frac{1}{2}\mathbf{T}_{\mathrm{up}} \\ \mathbf{T}_{q-} = \frac{1}{2j}\mathbf{T}_{\mathrm{dw}} - \frac{1}{2j}\mathbf{T}_{\mathrm{up}}. \end{cases} \tag{38}$$

The latter in (36), $T_{dq-}(\omega_1 t + 90^\circ)x_{dq}\Delta\theta$, can be written into HSS by (13) as $\mathbf{x}'_{d-}\Delta\boldsymbol{\theta}$ and $\mathbf{x}'_{q-}\Delta\boldsymbol{\theta}$.

Based on this, IPT time-domain expression (36) is transformed to HSS as

$$\Delta\mathbf{x} = \mathbf{T}_{d-}\Delta\mathbf{x}_d + \mathbf{T}_{q-}\Delta\mathbf{x}_q + \left(\mathbf{x'}_{d-} + \mathbf{x'}_{q-}\right)\Delta\boldsymbol{\theta}. \tag{39}$$

The HSS models in (35) and (39) show that the results of the PT and IPT contain two parts. One part is the perturbation of the input signal itself, which will be shifted by the $\mathbf{T}_{d+}$, $\mathbf{T}_{q+}$, $\mathbf{T}_{d-}$, and $\mathbf{T}_{q-}$. And the other part is the effect of the phase angle produced by the PLL. When PLL is ignored, $\Delta\boldsymbol{\theta}$ equals 0. The separation of the d- and q-axis signals in the models is beneficial to connect the ac current inner loop and the dc voltage outer loop (as shown in Fig. 4), so that the model can visually reflect the structure of the dual-loop controllers and has clear physical meaning.

B. HSS Model of PLL

Sun [11] gave the transfer function of the PLL under PS and NS perturbations, that is

$$\Delta\theta\left(\omega\right) = \frac{\mp jT_{\mathrm{PLL}}\left(\omega\right)}{1 + U_{\mathrm{ac1}}e^{\pm j\varphi}T_{\mathrm{PLL}}\left(\omega\right)}\Delta u_{\mathrm{ac}}\left(\omega \pm \omega_1\right) \tag{40}$$

where $t_{\mathrm{PLL}}(\omega)$ denotes the open-loop gain of the PLL that consists of PI controller and the integral link $1/s$; $u_{\mathrm{ac1}}e^{\pm j\varphi}$ is the steady-state voltage of the point of common coupling (PCC). Equation (40) shows that PLL will also shift the frequency according to the sequence of the perturbations as the PLL includes a PT. Therefore, the sequence abstraction matrix and the frequency shift matrix are also introduced in HSS modeling procedure for PLL, we have

$$\begin{aligned} \Delta\boldsymbol{\theta} &= \left[\mathbf{G}_{\mathrm{PLLp}}\mathbf{T}_{\mathrm{dw}}\mathbf{E}_+^s + \mathbf{G}_{\mathrm{PLLn}}\mathbf{T}_{\mathrm{up}}\mathbf{E}_-^s\right]\Delta\mathbf{u}_{\mathrm{ac}} \\ &= \mathbf{G}_{\mathrm{PLL}}\Delta\mathbf{u}_{\mathrm{ac}} \end{aligned} \tag{41a}$$

in which

$$\Delta\mathbf{u}_{\mathrm{ac}} = \Delta\mathbf{u}_{\mathrm{gac}} - \mathbf{Z}_{\mathrm{gac}}\mathbf{E}_{\pm}^s\Delta\mathbf{i}_{\mathrm{ac}} \tag{41b}$$

$$\begin{aligned} \mathbf{G}_{\mathrm{PLLp/n}} = \mathrm{diag}\big[&\ldots, G_{\mathrm{PLLp/n}}\left(\omega_{p-2}\right), G_{\mathrm{PLLp/n}}\left(\omega_{p-1}\right), \\ &G_{\mathrm{PLLp/n}}\left(\omega_p\right), G_{\mathrm{PLLp/n}}\left(\omega_{p+1}\right), G_{\mathrm{PLLp/n}}\left(\omega_{p+2}\right), \ldots\big]. \end{aligned} \tag{41c}$$

$G_{\mathrm{PLLp}}(\omega)$ and $G_{\mathrm{PLLn}}(\omega)$ are PS and NS closed-loop transfer functions of the PLL, respectively, which correspond to the gains of $\Delta u_{\mathrm{ac}}(\omega_p \pm \omega_1)$ in (40). According to (41a) and (41b), the PLL is equivalent to an ac voltage feedforward link as the PCC voltage directly affects $\Delta\boldsymbol{\theta}$, and this voltage consists of the ac grid impedance. It implies that in addition to the internal harmonic interactions (as discussed in Section III), the PLL also introduces grid impedance coupling to the MMC. And the greater the PLL gain, the more severe the grid impedance coupling.

C. HSS Model of AC Current Inner Loop

Applying (35) and (39) to the ac current inner loop controller shown in Fig. 4(b), the HSS expression of DM modulation index can be obtained as

$$\begin{aligned} \Delta\mathbf{m}_{\mathrm{dm}} = &\mathbf{T}_{d-}\Delta\mathbf{m}_{\mathrm{dm}d} + \mathbf{T}_{q-}\Delta\mathbf{m}_{\mathrm{dm}q} \\ &+ \left(\mathbf{m}'_{\mathrm{dm}d-} + \mathbf{m}'_{\mathrm{dm}q-}\right)\Delta\boldsymbol{\theta} \end{aligned} \tag{42a}$$

where

$$\begin{cases} \Delta\mathbf{m}_{\mathrm{dm}d} = \mathbf{G}_i\left(\Delta\mathbf{i}_{d\mathrm{ref}} - \Delta\mathbf{i}_d\right) \\ \qquad\qquad = \mathbf{G}_i\left(\Delta\mathbf{i}_{d\mathrm{ref}} - \mathbf{T}_{d+}\Delta\mathbf{i}_{\mathrm{ac}} - \mathbf{i'}_{d+}\Delta\boldsymbol{\theta}\right) \\ \Delta\mathbf{m}_{\mathrm{dm}q} = -\mathbf{G}_i\Delta\mathbf{i}_q = -\mathbf{G}_i\left(\mathbf{T}_{q+}\Delta\mathbf{i}_{\mathrm{ac}} + \mathbf{i'}_{q+}\Delta\boldsymbol{\theta}\right). \end{cases} \tag{42b}$$

$\mathbf{G}_i$ is the transfer function matrix related to the ac current PI controller, which has the similar diagonal structure to (41c), and $\Delta\mathbf{i}_{d\mathrm{ref}}$ denotes the perturbation of d-axis current reference generated by the dc voltage outer loop. The ac current controller can help to suppress the MMC current harmonics, which causes the grid impedance coupling. Therefore, the increase in current controller gain can reduce the degree of the grid impedance coupling.

D. HSS Model of DC Voltage Outer Loop

In dual-loop controllers, the dc voltage is controlled by adjusting the d-axis current. The HSS model of the dc voltage loop should reflect the transfer relationship between the dc voltage and the d-axis reference current. The dc terminal voltage of

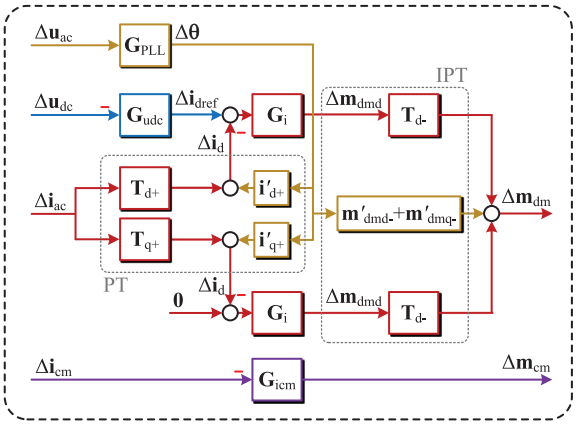

Fig. 5. Block diagram of the overall HSS model of MMC controllers.

MMC is calculated by

$$\Delta\mathbf{u}_{\rm dc}=\Delta\mathbf{u}_{\rm gdc}-\mathbf{Z}_{\rm gdc}\Delta\mathbf{i}_{\rm dc}=\Delta\mathbf{u}_{\rm gdc}-3\mathbf{Z}_{\rm gdc}\mathbf{E}_0^s\Delta\mathbf{i}_{\rm cm}. \tag{43}$$

From Fig. 4(b), this dc voltage perturbation can directly generate the reference for the ac current inner loop, that is

$$\Delta\mathbf{i}_{d\rm ref}=-\mathbf{G}_{u\rm dc}\Delta\mathbf{u}_{\rm dc} \tag{44}$$

where the negative sign comes from the negative feedback structure and $\mathbf{G}_{u\rm dc}$ is constituted by the transfer function of dc voltage outer loop controller with the diagonal structure as (41c). Obviously, the dc voltage controller introduces the dc grid impedance into the MMC model. Therefore, the grid impedance coupling on the MMC dc side will be enhanced by dc voltage controller. This coupling, as discussed in Section III, is so small that can be neglected on the dc side. However, the dc voltage outer loop will also strengthen the grid impedance coupling on the MMC ac side. This is because the $\Delta\mathbf{i}_{d\rm ref}$ generated by the dc voltage controller will enter the ac current inner loop and cause additional harmonics into $\Delta\mathbf{m}_{\rm dm}$ through the frequency shift effect of $\mathbf{T}_{d-}$, as shown in (42). These harmonics in $\Delta\mathbf{m}_{\rm dm}$ leads to ac harmonic currents on the MMC, thereby enhancing the ac grid impedance coupling.

E. HSS Model of the Circulating Current Controller

The circulating current fluctuation in MMC is suppressed by a proportional resonance (PR) controller in Fig. 4(c), and the CM modulation index is then produced. The HSS model of this control loop can be easily obtained according to the previous modeling procedure as

$$\Delta\mathbf{m}_{\rm cm}=-\mathbf{G}_{i\rm cm}\Delta\mathbf{i}_{\rm cm}. \tag{45}$$

where $\mathbf{G}_{i\rm cm}$ consists of the transfer function of PR controller.

F. Overall MMC Closed-Loop Impedance Model

Combining (41)–(45) leads to the overall HSS model of MMC controllers, which is presented as the block diagram shown in Fig. 5. Each matrix derived in Section IV can be found one-to-one in this block diagram; and the color of the block corresponds to the control loops of the control strategies drawn in Fig. 4, presenting a clear physical meaning of the proposed model. After simplifying the expression, the controller model can be written as

$$\underbrace{\begin{bmatrix}\Delta\mathbf{m}_{\rm cm}\\ \Delta\mathbf{m}_{\rm dm}\end{bmatrix}}_{\Delta\mathbf{m}}=\underbrace{\begin{bmatrix}\mathbf{G}_{\rm fb11}&0\\0&\mathbf{G}_{\rm fb22}\end{bmatrix}}_{\mathbf{G}_{\rm fb}}\underbrace{\begin{bmatrix}\Delta\mathbf{i}_{\rm cm}\\ \Delta\mathbf{i}_{\rm ac}\end{bmatrix}}_{\Delta\mathbf{i}}+\underbrace{\begin{bmatrix}0&0\\\mathbf{G}_{\rm ff21}&\mathbf{G}_{\rm ff22}\end{bmatrix}}_{\mathbf{G}_{\rm ff}}\underbrace{\begin{bmatrix}\Delta\mathbf{u}_{\rm dc}\\ \Delta\mathbf{u}_{\rm ac}\end{bmatrix}}_{\Delta\mathbf{u}}. \tag{46a}$$

where

$$\begin{cases}\mathbf{G}_{\rm fb11}=-\mathbf{G}_{i\rm cm}\\ \mathbf{G}_{\rm fb22}=-(\mathbf{T}_{d-}\mathbf{G}_i\mathbf{T}_{d+}+\mathbf{T}_{q-}\mathbf{G}_i\mathbf{T}_{q+})\\ \mathbf{G}_{\rm ff21}=-\mathbf{T}_{d-}\mathbf{G}_i\mathbf{G}_{u\rm dc}\\ \mathbf{G}_{\rm ff22}=[-\mathbf{T}_{d-}\mathbf{G}_i\mathbf{i}'_{d+}-\mathbf{T}_{q-}\mathbf{G}_i\mathbf{i}'_{q+}\\ \qquad\qquad+(\mathbf{m}'_{{\rm dm}d-}+\mathbf{m}'_{{\rm dm}q-})]\,\mathbf{G}_{\rm PLL}\\ \Delta\mathbf{u}=\Delta\mathbf{u}_{\rm g}-\mathbf{Z}_{\rm g}\Delta\mathbf{i}\end{cases} \tag{46b}$$

where $\mathbf{G}_{\rm fb}$ is the feedback matrix, which reflects the regulation of ac current and circulating current controller. The diagonal structure of $\mathbf{G}_{\rm fb}$ indicates that the circulating current and the ac current control of MMC are independent of each other. $\mathbf{G}_{\rm ff}$ denotes the feedforward matrix that contains PLL and dc voltage outer loop control, reflecting the influence of terminal voltage on the MMC. Substituting (46) into MMC open-loop model (24a), a complete HSS-based MMC model under closed-loop condition is finally derived as

$$\Delta\mathbf{u}_{\rm g}=\left(\mathbf{I}-\mathbf{K}_m\mathbf{G}_{\rm ff}\right)^{-1}\left[\mathbf{K}_i+\mathbf{Z}_{\rm g}+\mathbf{K}_m\left(\mathbf{G}_{\rm fb}-\mathbf{G}_{\rm ff}\mathbf{Z}_{\rm g}\right)\right]\Delta\mathbf{i}. \tag{47}$$

The ac and dc impedances of the closed-loop MMC can be obtained by solving (47) and substituting results into (26) and (27). A detailed example to help readers understand the modeling procedure is presented in the Appendix. This model not only reveals the grid impedance coupling of MMC, but also synthesize a variety of complex control links with clear physical meaning, including but not limited to PLL, dual-loop controllers, and circulating current controller. Furthermore, it gives a unified MMC modeling method, which is suitable for both dc and ac impedances, providing a flexible and accurate way to analyze the stability and dynamic characteristics of MMC.

V. Verification

A. Verification of the Sequence Analysis Results

With the parameters given in Table II, the analysis of MMC frequency and sequence in Section III are proved by the simulation based on MATLAB/Simulink. A 1-kV, 40-Hz perturbation voltage was injected into different positions of the MMC, and the first three harmonics (ω_p, $\omega_p\pm\omega_1$, $\omega_p\pm2\omega_1$, $\omega_p\pm3\omega_1$) of responses are listed in Table III.

TABLE II
SIMULATION PARAMETERS

Parameters	Value
Rated power	P_N=400 MW
Dc voltage	u_{gdc}=400 kV
Ac line-to-line RMS voltage	$u_{gac(rms)}$=220 kV
The number of SMs	N=250
SM capacitance	C=12 mF
Arm inductance	L=90 mH
Arm equivalent resistance	R=1 Ω
Ac grid impedance	R_{gac}=12 Ω, L_{gac}=194 mH
Dc grid impedance	R_{gdc}=0.095 Ω, L_{gdc}=41 mH
PI controller of PLL	K_{pPLL}=0.0005, K_{iPLL}=0.001
PI controller of ac current loop	K_{piac}=0.0001, K_{iiac}=0.004
PI controller of dc voltage loop	K_{pudc}=0.005, K_{iudc}=0.005
PR controller of circulating current	K_{picm}=0.00005, K_{ricm}=0.002, ω_r=200π rad/s, ω_c=10 rad/s

When the perturbation is injected from ac side, in addition to the 40-Hz response in $i_{\rm ac}$, the coupling current of other frequency also appears. As shown in Table III(a), when a PS perturbation is injected, the NS coupling current appears at -60 Hz with the magnitude of 2.5 A, whereas in Table III(b), the NS perturbation causes the PS coupling current at 140 Hz with the magnitude of 0.03 A. It can be seen that as the harmonic order increases, the amplitude of each response decreases significantly, and the results more than third harmonics are negligible. For e.g., the harmonic of $i_{\rm ac}$ at 240 Hz ($\omega_p + 4\omega_1$, which is not listed) caused by PS perturbation voltage is only about 0.0002 A. These coupling currents will generate voltages on the ac grid impedance and be reflected back to the MMC, which further affects the MMC ac impedance. In terms of dc side, as shown in Table III(c), the injected perturbation produces only a 28.9-A, 40-Hz response in $i_{\rm dc}$, without coupling currents at other frequencies (within first three harmonics). Thus, the grid impedance coupling on the MMC dc side is much weaker than that on the ac side. The simulation results are consistent with the discussions presented in Section III.

B. Verification of the MMC Impedance Models

The accuracy of the MMC impedance model is verified in this section. Both the ac and dc impedances of MMC are solved by the model (47). For comparison, with the same parameters, an MMC circuit is simulated, and its impedance is measured by frequency sweep in MATLAB/Simulink.

Fig. 6 shows the Bode plots of the MMC ac and dc impedances under different control strategies. The solid line denote the impedance calculated by HSS, whereas the data obtained from sweeping are marked in the figure by circles or diamonds. Obviously, the results of the MMC impedance model are satisfactorily fitted with the sweeping data, showing the high accuracy of the proposed model. Observing from Fig. 6(a), both MMC ac and dc impedances contain many resonant peaks under open-loop operation, indicating that these resonances are caused by the passive components and MMC frequency coupling. When a PR circulating current controller is added, these resonance peaks are effectively suppressed, as shown in Fig. 6(b). It can be seen that the circulating current control weakens most of the resonances in the ac impedance, leaving only a series resonant peak at around 38 Hz generated by MMC passive components. And for the dc impedance, the circulating current controller introduces an additional 100 Hz resonance peak, because the PR controller has the strongest control effect on the dc current at 100 Hz, and the suppression of the current perturbation increases the equivalent impedance. With addition of the ac current PI controller, a significant difference between the PS and NS impedances has emerged in the middle-frequency range, as plotted in Fig. 6(c). The PS impedance has an obvious resonance peak at 50 Hz due to the control effect of the ac current loop. This resonance peak is even large enough to mask series resonance caused by passive components at 38 Hz. However, this current controller has weaker ability to regulate the NS current, so the NS impedance is significantly lower than the PS impedance around 50 Hz. Furthermore, after adding PLL, the phase angle used for PT and IPT will deviate from steady-state values due to the ac voltage perturbation, thereby weakening the control ability of the ac current loop, as shown in Fig. 6(d); thus, the resonant peak of ac impedance at 50 Hz is reduced. Since the ac current controller and PLL do not directly act on the dc current, they have less impact on the MMC dc impedance. In contrast, the dc voltage controller has a greater impact on dc impedance than ac impedance. Compared with Fig. 6(d), the dc impedance in Fig. 6(e) decreases as the frequency goes down in a range below 0.2 Hz (the corner frequency of the dc voltage controller). This is because the behavior of MMC dc side is expected as a voltage source at low-frequency range under the dc voltage control. It can be seen that ac impedance is hardly affected by the dc voltage loop due to a small bandwidth of the controller, which is, however, sufficient to maintain the voltage control performance in this case.

C. Factors Affecting the Grid Impedance Coupling

In order to demonstrate the influence of different factors on the grid impedance coupling effect, Fig. 7 represents the coupling degree by using the error between the MMC ac impedance with and without considering the coupling.

Fig. 7(a) and (b) shows the variations of the grid impedance coupling when the controller gains of dc voltage loop and PLL are changed, respectively. Both the gains of the dc voltage controller and the PLL exacerbate the coupling, and the coupling caused by PLL is more severe than dc voltage controller. It is consistent with the description in (41b) that the PLL is equivalent to an ac voltage feedforward link, which directly introduces the grid impedance into MMC. Fig. 7(c) shows that a higher ac current gain results in a smaller coupling. This is because the increase in the ac current controller gain can help to reduce the MMC current harmonics, which has been pointed out in Section IV. In Fig. 7(d), the influence of different grid impedances on the coupling is demonstrated. The MMC is connected to the grid with short-circuit ratio (SCR) varying from

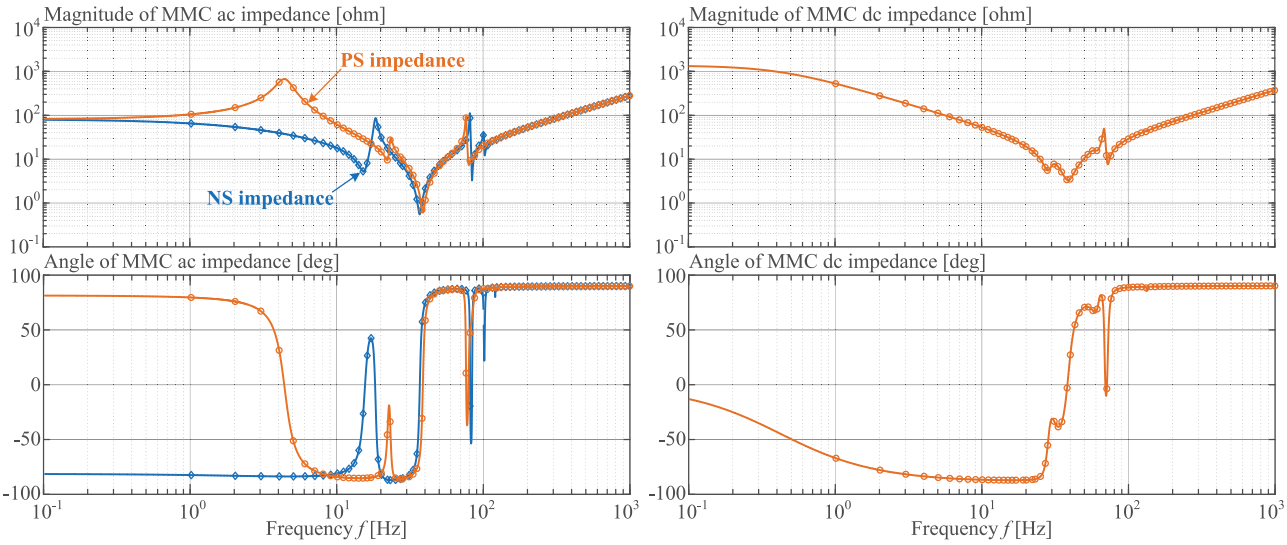

(a)

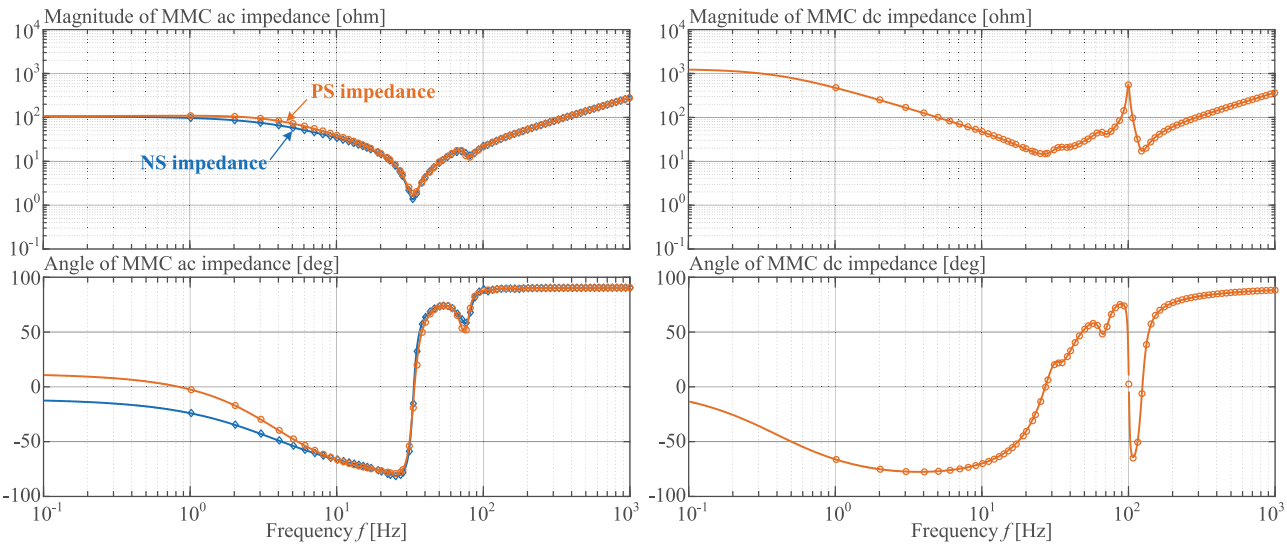

(b)

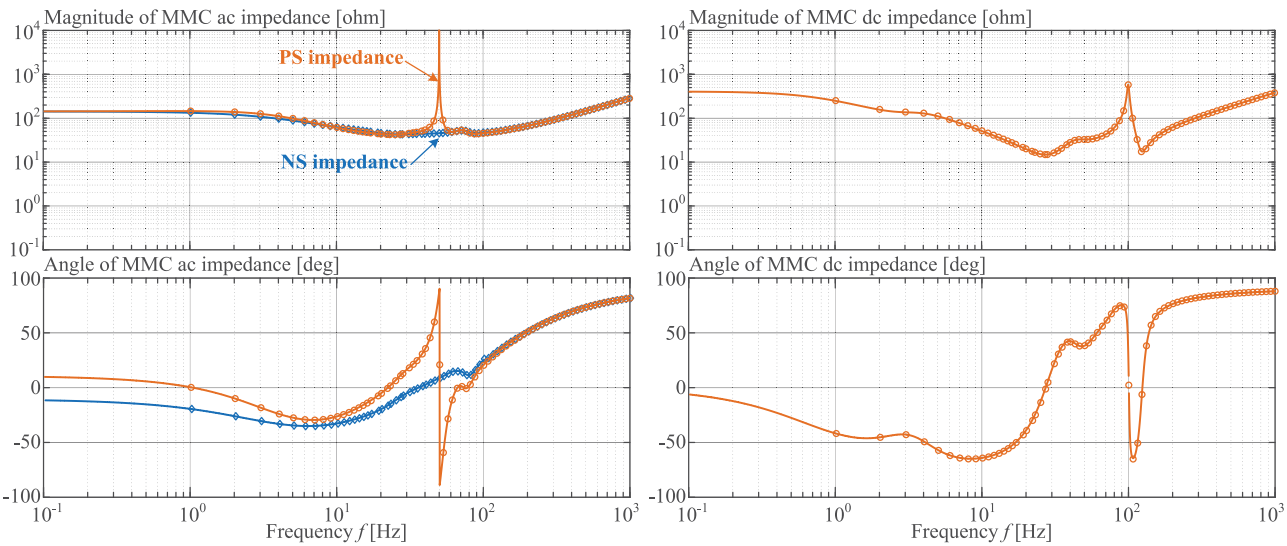

(c)

Fig. 6. MMC ac and dc impedances with different control strategies. (a) Under open-loop condition ($m_{\mathrm{cm}} = 0.5, m_{\mathrm{dm}} = 0.43\cos(\omega_1 t - 4.6°)$). (b) Add circulating current control. (c) Add ac current control. (d)Add PLL. (e) Add dc voltage control.

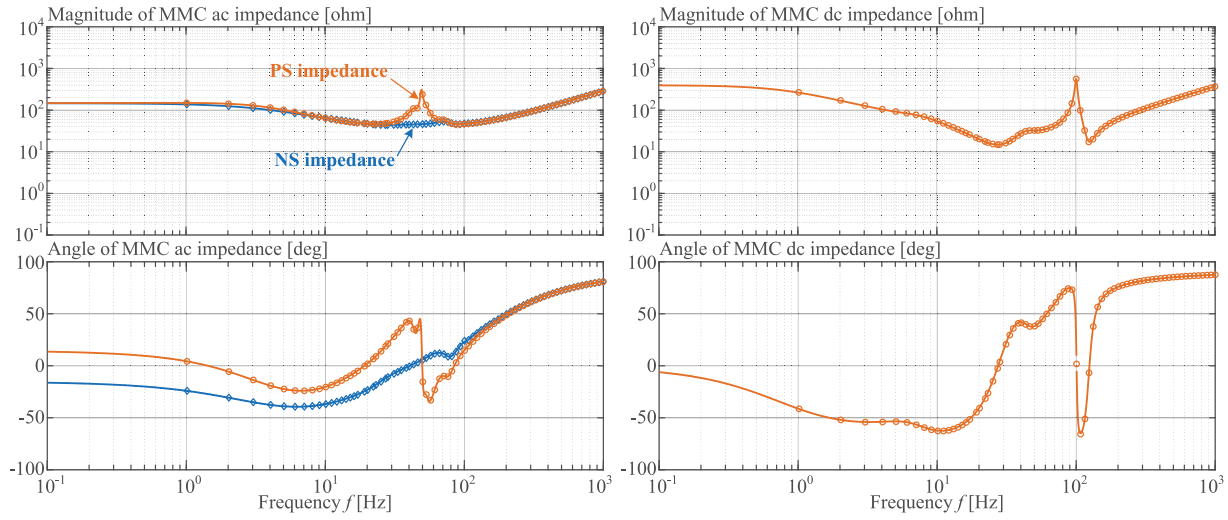

(d)

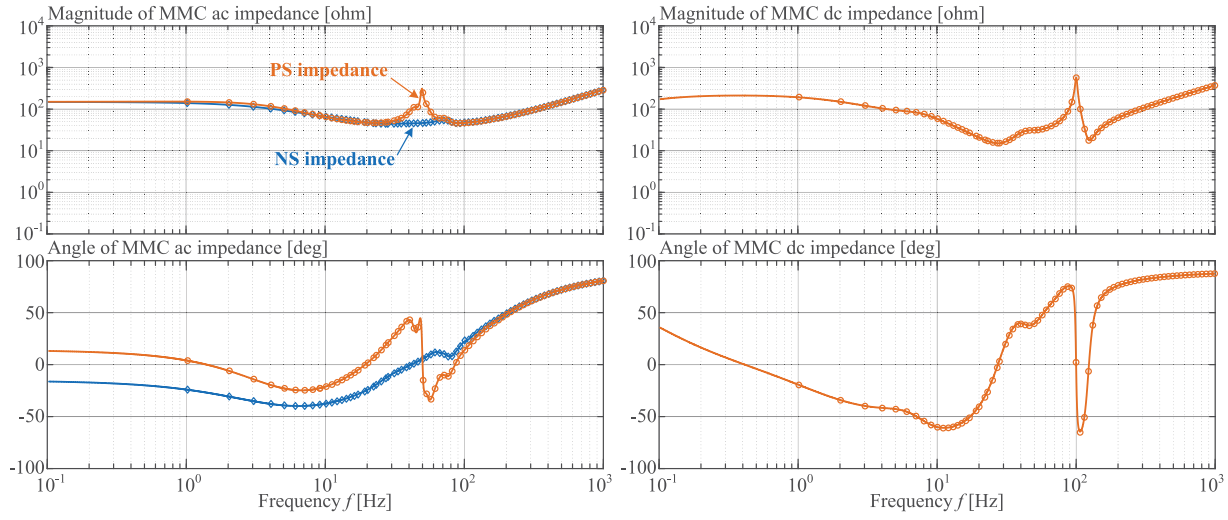

(e)

Fig. 6. Continued.

TABLE III
SIMULATION (FFT RESULTS) WITH INJECTION OF DIFFERENT PERTURBATIONS

Case	Freq. [Hz]	i_{cm} [A]			i_{dc} [A]	i_{ac} [A]			u_{Ccm} [V]			u_{Cdm} [V]		
		A	B	C		A	B	C	A	B	C	A	B	C
(a)	-110	0.2(-23°)	0.2(-143°)	0.2(97°)					0.04(-168°)	0.04(72°)	0.04(-48°)			
	-60					**2.5(66°)**	**2.5(-174°)**	**2.5(-54°)**				0.1(-163°)	0.1(-43°)	0.1(77°)
	-10	2.6(-178°)	2.6(-178°)	2.6(-178°)	7.7(-178°)				0.8(-26°)	0.8(-26°)	0.8(-26°)			
	40					**7.6(-56°)**	**7.6(-176°)**	**7.6(64°)**				0.5(-179°)	0.5(61°)	0.5(-59°)
	90	0.3(-45°)	0.3(75°)	0.3(-165°)					0.2(-134°)	0.2(-14°)	0.2(106°)			
	140											0.009(-98°)	0.009(-98°)	0.009(-98°)
	190	0.01(34°)	0.01(-86°)	0.01(154°)					0.001(-52°)	0.001(-172°)	0.001(69°)			
(b)	-110	0.1(12°)	0.1(132°)	0.1(-108°)					0.01(109°)	0.01(-131°)	0.01(-11°)			
	-60											0.2(-109°)	0.2(-109°)	0.2(-109°)
	-10	3.9(157°)	3.9(37°)	3.9(-83°)					0.8(-21°)	0.8(-141°)	0.8(99°)			
	40					**13.4(-40°)**	**13.4(80°)**	**13.4(-161°)**				0.7(-133°)	0.7(-13°)	0.7(107°)
	90	0.4(-35°)	0.4(-35°)	0.4(-35°)	1.2(-35°)				0.3(-135°)	0.3(-135°)	0.3(-135°)			
	140					**0.03(175°)**	**0.03(55°)**	**0.03(-66°)**				0.01(-92°)	0.01(148°)	0.01(28°)
	190	0.02(48°)	0.02(168°)	0.02(-72°)					0.003(-30°)	0.003(90°)	0.003(-150°)			
(c)	-110											0.08(-49°)	0.08(-49°)	0.08(-49°)
	-60	3(-135°)	3(105°)	3(-15°)					0.5(-61°)	0.5(179°)	0.5(59°)			
	-10					6.6(176°)	6.6(-64°)	6.6(56°)				2.7(-13°)	2.7(107°)	2.7(-133°)
	40	9.6(-53°)	9.6(-53°)	9.6(-53°)	**28.9(-53°)**				1.3(-151°)	1.3(-151°)	1.3(-151°)			
	90					0.6(8°)	0.6(-113°)	0.6(128°)				0.4(-140°)	0.4(100°)	0.4(-20°)
	140	0.6(-5°)	0.6(116°)	0.6(-125°)					0.05(-88°)	0.05(32°)	0.05(152°)			
	190											0.01(-105°)	0.01(-105°)	0.01(-105°)

Note: (a) Inject 1-kV, 40-Hz PS perturbation voltage intoac side. (b) Inject 1-kV, 40-Hz NS perturbation voltage into ac side. (c) Inject 1-kV, 40-Hz perturbation voltage into dc side.

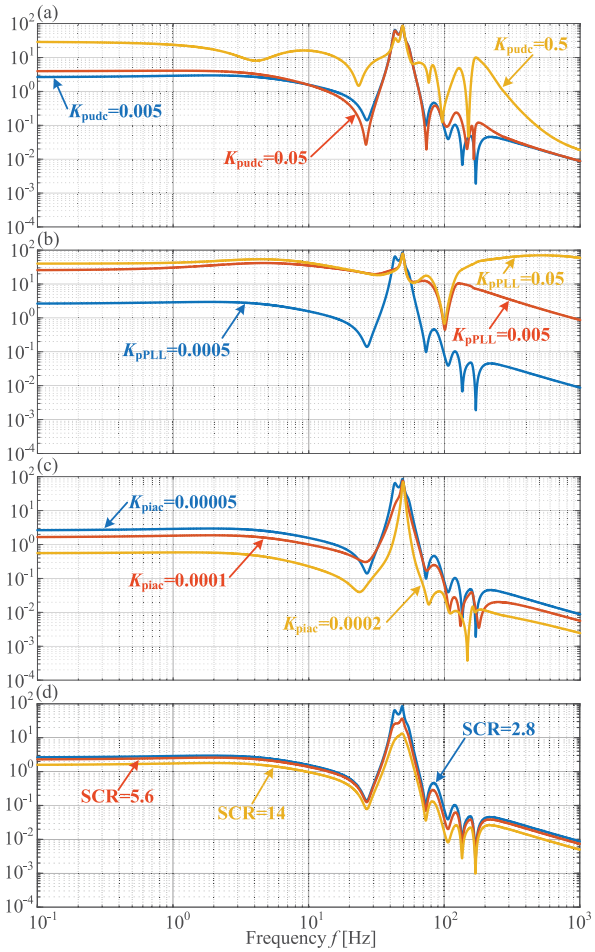

Fig. 7. Coupling degree under different conditions. (a) Coupling degree under different dc voltage controller gains [ohm]. (b) Coupling degree under different PLL gains [ohm]. (c) Coupling degree under different ac current controller gains [ohm]. (d) Coupling degree under different ac grid impedance [ohm].

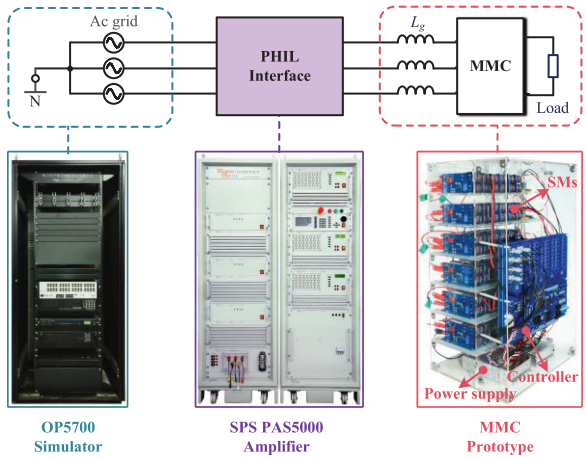

Fig. 8. Prototype structure for power hardware in the loop experiment.

TABLE IV
EXPERIMENTAL PARAMETERS

Parameters	Value
Dc voltage	u_{gdc}=300 V
Ac phase-to-ground voltage	u_{gac}=140 V
The number of SMs	N=6
SM capacitance	C=2.04 mF
Arm inductance	L=4 mH
Arm equivalent resistance	R=0.8 Ω
Ac grid impedance	L_{gac}=16 mH
Dc grid impedance (load)	R_{gdc}=40 Ω
PI controller of PLL	K_{pPLL}=0.1, K_{iPLL}=0.5
PI controller of ac current loop	K_{piac}=0.007, K_{iiac}=0.5
PI controller of dc voltage loop	K_{pudc}=0.2, K_{iudc}=7
PR controller of circulating current	K_{picm}=0, K_{ricm}=0.2, ω_r=200π rad/s, ω_c=10 rad/s

2.8 (R_{gac} = 12 Ω, L_{gac} = 194 mH) to 14 (R_{gac} = 2.4 Ω, L_{gac} = 38.8 mH). And the results show that the weaker the grid connected to the MMC, the more severe the coupling degree.

The variation of the coupling degree shown in the simulation is closely consistent with the model analysis results. It indicates that the proposed MMC impedance model, which considers the grid impedance coupling, can improve the analysis accuracy, especially in the case where dc voltage loop and PLL gain are large, ac current loop gain is small, or MMC is connected to a weak grid.

D. Stability Analysis Example

This section demonstrates the impact of the grid impedance coupling on MMC stability analysis by experimental verifications based on power hardware-in-the-loop (PHIL). The structure of the platform is given in Fig. 8, where the ac grid is emulated in a real-time simulator and is connected with a downscaled MMC prototype through a power amplifier. The experimental parameters are listed in Table IV.

Fig. 9 represents the experimental waveforms under different controller gains. At instant t_1, the ac current controller gain k_{piac} is reduced from 0.02 to 0.007, and the MMC waveforms gradually oscillate. The fast Fourier transform (FFT) plot of unstable ac current is further drawn in Fig. 10, which shows that the oscillation frequency appears at 55.7 Hz. After t_2, the gain is changed back to 0.02, and the MMC become restable. This experimental result is consistent with the stability analysis based on the proposed complete MMC impedance model. As shown in Fig. 11, the orange and purple curves correspond to the MMC ac impedance by setting the ac current controller gain to 0.007 and 0.02, respectively. The purple circles marked on the impedance curve denote the frequency sweep data obtained from the PHIL experiment, ensuring the accuracy of the model. By applying Nyquist criteria between the MMC and the grid impedance, the orange curve (k_{piac} = 0.007) intersects the grid impedance at 57.3 Hz with the phase margin less than zero, which is unstable. And the purple curve predicts the MMC stable operation due to its phase margin of 31.2°. For comparison, the ac impedance (k_{piac} = 0.007) ignoring the grid impedance coupling is also drawn in Fig. 11 with blue lines. This model, however, leads to an erroneous stability analysis result. The comparison not

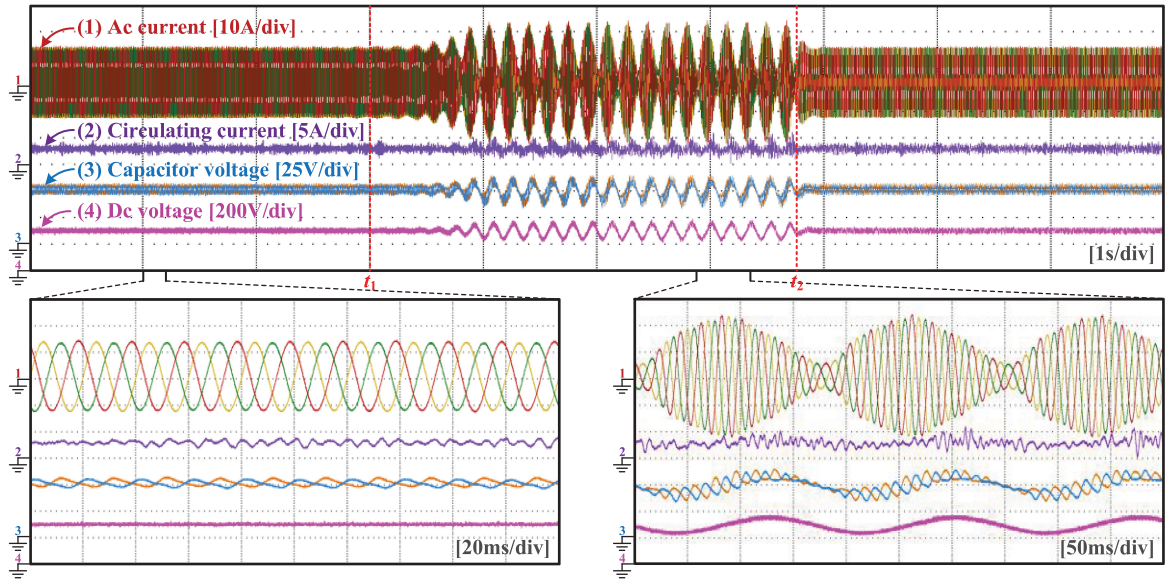

Fig. 9. Experimental results under different controller parameters.

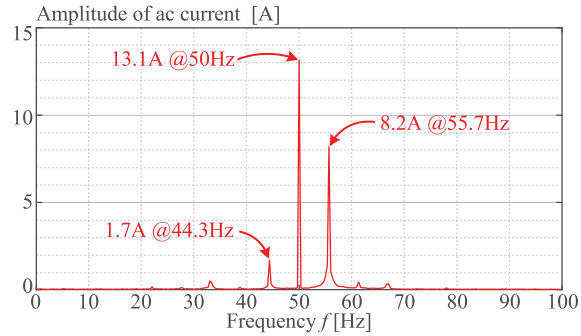

Fig. 10. FFT results of experimental unstable ac current.

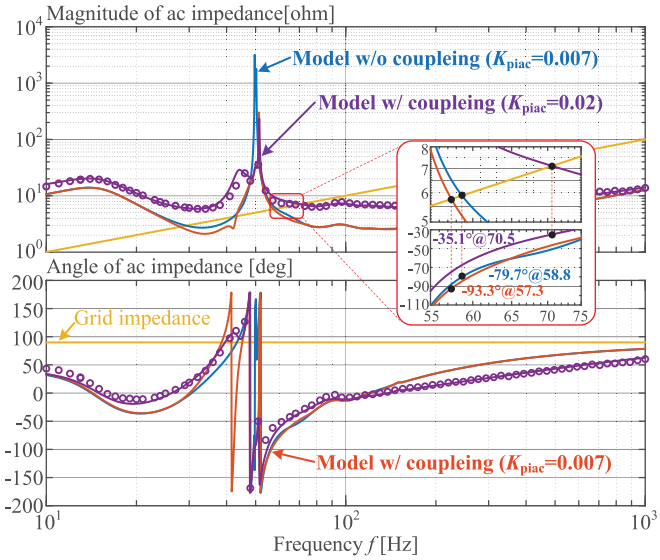

Fig. 11. Comparison of stability analysis with and without considering the grid impedance coupling.

only verifies the accuracy of the proposed MMC model, but also reflects the necessity of considering grid impedance coupling in MMC stability analysis.

VI. Conclusion

The impedance model is the most common method for grid-connected stability analysis. This article proposes a complete MMC impedance model based on HSS, which has high accuracy and reveals the grid impedance coupling of MMC. Moreover, the proposed model not only consists of the ac current and the circulating current control, but also incorporates dc voltage outer loop and PLL. By introducing the frequency shift matrix and the sequence extraction matrix, the MMC model is more concise and thus easily reflects the clear physical meaning. This model indicates that the coupling can be increased by higher dc voltage loop and PLL gains, smaller current loop gains, and weaker grids. In these cases, it is necessary to use the proposed model to improve the analysis accuracy. Finally, correctness of the model is substantiated by simulation and experimental results.

Appendix

This appendix gives an example to derive the MMC PS impedance at the perturbation frequency $f_p = 40$ Hz step by step. All parameters in this example are based on Table II.

First, the steady-state operating point is the basis of the small-signal model. It consists of CM and DM modulation indexes ($m_{\rm cm}$, $m_{\rm dm}$), CM and DM capacitor voltages ($u_{\rm Ccm}$, $u_{\rm Cdm}$), circulating current ($i_{\rm cm}$), ac current ($i_{\rm ac}$), and ac terminal PCC voltage ($u_{\rm ac}$). These steady-state values can be obtained by solving MMC nonlinear equations, or they can be measured by simulation or experiment. Table V shows all these steady-state values of phase A, where only the first two harmonics are considered in this example due to the page limitation.

TABLE V
STEADY-STATE VALUES OF PHASE A ($\omega_1 = 2\pi f_1 = 314$ rad/s)

Values
m_{cm}=0.48+0.01cos(2$\omega_1 t$+83.5°)
m_{dm}=0.43cos($\omega_1 t$−4.6°)
u_{Ccm}=1653.8 V+21.2cos(2$\omega_1 t$−95.8°) V
u_{Cdm}=57.9cos($\omega_1 t$−86°) V
i_{cm}=−330 A+6.7cos(2$\omega_1 t$+84.5°) A
i_{ac}=1484.8cos($\omega_1 t$−0.5°) A
u_{ac}=178890cos($\omega_1 t$−0.5°) V

By substituting the values of Table V into the structure of Toeplitz matrix shown in (13), the steady-state variables matrixes in (24b) and (24c) could be obtained as (a1)–(a6), as shown at the bottom of the page.

Second, the block matrixes in (24), such as $\mathbf{K}_i$, $\mathbf{K}_m$, $\Delta\mathbf{S}$, $3\mathbf{Z}_{\rm gdc}\mathbf{E}_0^+$ and $\mathbf{Z}_{\rm gac}\mathbf{E}_\pm^+$, are required to form the impedance model of MMC. Among them, $\mathbf{K}_i$ and $\mathbf{K}_m$ could be calculated as (a7)–(a14), as shown at the bottom of the next page.

With a PS perturbation frequency $f_p = 40$ Hz, the matrix $\Delta\mathbf{S}$ could be obtained by substituting $p = 0.8$ ($f_p/f_1 = 0.8$) into

$$\mathbf{m}_{\rm cm} = \begin{bmatrix} 0.48\angle 0^\circ & 0 & \frac{0.01\angle -83.5^\circ}{2} & 0 & 0 \\ 0 & 0.48\angle 0^\circ & 0 & \frac{0.01\angle -83.5^\circ}{2} & 0 \\ \frac{0.01\angle 83.5^\circ}{2} & 0 & 0.48\angle 0^\circ & 0 & \frac{0.01\angle -83.5^\circ}{2} \\ 0 & \frac{0.01\angle 83.5^\circ}{2} & 0 & 0.48\angle 0^\circ & 0 \\ 0 & 0 & \frac{0.01\angle 83.5^\circ}{2} & 0 & 0.48\angle 0^\circ \end{bmatrix} \tag{a1}$$

$$\mathbf{m}_{\rm dm} = \begin{bmatrix} 0 & \frac{0.43\angle 4.6^\circ}{2} & 0 & 0 & 0 \\ \frac{0.43\angle -4.6^\circ}{2} & 0 & \frac{0.43\angle 4.6^\circ}{2} & 0 & 0 \\ 0 & \frac{0.43\angle -4.6^\circ}{2} & 0 & \frac{0.43\angle 4.6^\circ}{2} & 0 \\ 0 & 0 & \frac{0.43\angle -4.6^\circ}{2} & 0 & \frac{0.43\angle 4.6^\circ}{2} \\ 0 & 0 & 0 & \frac{0.43\angle -4.6^\circ}{2} & 0 \end{bmatrix} \tag{a2}$$

$$\mathbf{u}_{\rm Ccm} = \begin{bmatrix} 1653.8\angle 0^\circ & 0 & \frac{21.2\angle 95.8^\circ}{2} & 0 & 0 \\ 0 & 1653.8\angle 0^\circ & 0 & \frac{21.2\angle 95.8^\circ}{2} & 0 \\ \frac{21.2\angle -95.8^\circ}{2} & 0 & 1653.8\angle 0^\circ & 0 & \frac{21.2\angle 95.8^\circ}{2} \\ 0 & \frac{21.2\angle -95.8^\circ}{2} & 0 & 1653.8\angle 0^\circ & 0 \\ 0 & 0 & \frac{21.2\angle -95.8^\circ}{2} & 0 & 1653.8\angle 0^\circ \end{bmatrix} \tag{a3}$$

$$\mathbf{u}_{\rm Cdm} = \begin{bmatrix} 0 & \frac{57.9\angle 86^\circ}{2} & 0 & 0 & 0 \\ \frac{57.9\angle -86^\circ}{2} & 0 & \frac{57.9\angle 86^\circ}{2} & 0 & 0 \\ 0 & \frac{57.9\angle -86^\circ}{2} & 0 & \frac{57.9\angle 86^\circ}{2} & 0 \\ 0 & 0 & \frac{57.9\angle -86^\circ}{2} & 0 & \frac{57.9\angle 86^\circ}{2} \\ 0 & 0 & 0 & \frac{57.9\angle -86^\circ}{2} & 0 \end{bmatrix} \tag{a4}$$

$$\mathbf{i}_{\rm cm} = \begin{bmatrix} 330\angle 180^\circ & 0 & \frac{6.7\angle -84.5^\circ}{2} & 0 & 0 \\ 0 & 330\angle 180^\circ & 0 & \frac{6.7\angle -84.5^\circ}{2} & 0 \\ \frac{6.7\angle 84.5^\circ}{2} & 0 & 330\angle 180^\circ & 0 & \frac{6.7\angle -84.5^\circ}{2} \\ 0 & \frac{6.7\angle 84.5^\circ}{2} & 0 & 330\angle 180^\circ & 0 \\ 0 & 0 & \frac{6.7\angle 84.5^\circ}{2} & 0 & 330\angle 180^\circ \end{bmatrix} \tag{a5}$$

$$\mathbf{i}_{\rm ac} = \begin{bmatrix} 0 & \frac{1484.8\angle 0.5^\circ}{2} & 0 & 0 & 0 \\ \frac{1484.8\angle -0.5^\circ}{2} & 0 & \frac{1484.8\angle 0.5^\circ}{2} & 0 & 0 \\ 0 & \frac{1484.8\angle -0.5^\circ}{2} & 0 & \frac{1484.8\angle 0.5^\circ}{2} & 0 \\ 0 & 0 & \frac{1484.8\angle -0.5^\circ}{2} & 0 & \frac{1484.8\angle 0.5^\circ}{2} \\ 0 & 0 & 0 & \frac{1484.8\angle -0.5^\circ}{2} & 0 \end{bmatrix} \tag{a6}$$

(15), that is

$$\Delta\mathbf{S} = \mathrm{diag}\left(-j376.8, -j62.8, j251.2, j565.2, j879.2\right). \tag{a15}$$

Matrixes $3\mathbf{Z}_{\mathrm{gdc}}\mathbf{E}_0^+$ and $\mathbf{Z}_{\mathrm{gac}}\mathbf{E}_\pm^+$ in (24a) are expressed as

$$3\mathbf{Z}_{\mathrm{gdc}}\mathbf{E}_0^+ = \mathrm{diag}\left(0, 0.285 - j7.73, 0, 0, 0.285 + j108.2\right) \tag{a16}$$

$$\mathbf{Z}_{\mathrm{gac}}\mathbf{E}_\pm^+ = \mathrm{diag}\left(12 - j73.1, 0, 12 + j48.8, 12 + j109.7, 0\right). \tag{a17}$$

In this example, the perturbation voltage are set as $\Delta u_{\mathrm{gdc}}(\omega_p) = 0$ and $\Delta u_{\mathrm{gac}}(\omega_p) = 1000$V, corresponding to vectors like

$$\Delta\mathbf{u}_{\mathrm{gdc}} = [0,0,0,0,0]^{\mathrm{T}}, \Delta\mathbf{u}_{\mathrm{gac}} = [0,0,1000,0,0]^{\mathrm{T}}. \tag{a18}$$

$$\mathbf{K}_{i\mathrm{cm1}} = \begin{bmatrix} 11.9\angle -80.3^\circ & 0 & 30.7\angle 99.4^\circ & 0 & 0.004\angle 103^\circ \\ 0 & 138.9\angle 89.2^\circ & 0 & 7.9\angle -70.4^\circ & 0 \\ 30.7\angle 80.6^\circ & 0 & 34.3\angle 86.7^\circ & 0 & 3.4\angle -89.4^\circ \\ 0 & 7.9\angle -109.6^\circ & 0 & 75\angle 88.5^\circ & 0 \\ 0.004\angle 77^\circ & 0 & 3.4\angle -90.6^\circ & 0 & 144\angle 89.2^\circ \end{bmatrix} \tag{a7}$$

$$\mathbf{K}_{i1} = \begin{bmatrix} 0 & 0 & 0 & 0.3\angle 11.1^\circ & 0 \\ 39.9\angle 85.3^\circ & 0 & 25.7\angle 94.6^\circ & 0 & 0 \\ 0 & 0 & 0 & 12.4\angle -83.9^\circ & 0 \\ 0.3\angle 168.9^\circ & 0 & 12.4\angle -96.1^\circ & 0 & 0 \\ 0 & 0 & 0 & 6.2\angle -93.8^\circ & 0 \end{bmatrix} \tag{a8}$$

$$\mathbf{K}_{i\mathrm{cm2}} = \begin{bmatrix} 0 & 39.9\angle 94.7^\circ & 0 & 0.3\angle 11.1^\circ & 0 \\ 39.9\angle 85.3^\circ & 0 & 25.7\angle 94.6^\circ & 0 & 0.1\angle -168.9^\circ \\ 0 & 25.7\angle 85.4^\circ & 0 & 12.4\angle -83.9^\circ & 0 \\ 0.3\angle 168.9^\circ & 0 & 12.4\angle -96.1^\circ & 0 & 6.2\angle -86.2^\circ \\ 0 & 0.1\angle -11.1^\circ & 0 & 6.2\angle -93.8^\circ & 0 \end{bmatrix} \tag{a9}$$

$$\mathbf{K}_{i2} = \begin{bmatrix} 3\angle -80.3^\circ & 0 & 7.7\angle 99^\circ & 0 & 0 \\ 0 & 0 & 0 & 2\angle -70.4^\circ & 0 \\ 7.7\angle 80.6^\circ & 0 & 8.6\angle 86.7^\circ & 0 & 0 \\ 0 & 0 & 0 & 19\angle 88.5^\circ & 0 \\ 0.001\angle 77^\circ & 0 & 0.9\angle -90.6^\circ & 0 & 0 \end{bmatrix} \tag{a10}$$

$$\mathbf{K}_{m\mathrm{cm1}} = \begin{bmatrix} 823.9\angle 2.5^\circ & 0 & 58.2\angle 94.7^\circ & 0 & 0.003\angle 102^\circ \\ 0 & 835.7\angle -7.5^\circ & 0 & 8\angle -76.8^\circ & 0 \\ 47.6\angle 84.4^\circ & 0 & 834.3\angle 5^\circ & 0 & 0.6\angle -108.5^\circ \\ 0 & 18.6\angle -91.6^\circ & 0 & 826.2\angle -0.4^\circ & 0 \\ 0.003\angle 78^\circ & 0 & 11.2\angle -96.4^\circ & 0 & 826.5\angle 0.1^\circ \end{bmatrix} \times 10^3 \tag{a11}$$

$$\mathbf{K}_{m\mathrm{dm1}} = \begin{bmatrix} 0 & 13.5\angle -71.4^\circ & 0 & 0.2\angle 15.7^\circ & 0 \\ 95.9\angle 89.1^\circ & 0 & 144.3\angle 90.4^\circ & 0 & 0.3\angle -171.6^\circ \\ 0 & 90.9\angle -92^\circ & 0 & 10\angle -82.9^\circ & 0 \\ 1.1\angle 173.3^\circ & 0 & 15.7\angle -87.6^\circ & 0 & 4.7\angle 81^\circ \\ 0 & 0.4\angle -7.5^\circ & 0 & 17.8\angle -84.6^\circ & 0 \end{bmatrix} \times 10^3 \tag{a12}$$

Substituting (a7)–(a18) into (24a), the ac current response $\Delta i_{\rm ac}(\omega_p)$ can be solved, which equals $(19.1\angle -76°)$ A. And according to (26), the MMC open-loop ac impedance at 40 Hz is

$$Z_{\rm ac\_MMC}(\omega_p)=\frac{1000}{19.1\angle -76°}-(12+j48.8)=2.07\angle 72°. \tag{a19}$$

Next, the HSS model of controllers are required to calculate the MMC closed-loop impedance. The transfer functions of these controllers are presented as

$$G_{\rm PLLp/n}(\omega)=\frac{\mp j\left[K_{\rm pPLL}+K_{\rm iPLL}/(j\omega)\right]}{j\omega_p+U_{\rm ac1}e^{\pm j\varphi}\left[K_{\rm pPLL}+K_{\rm iPLL}/(j\omega)\right]} \tag{a20}$$

$$G_{u\rm dc}(\omega)=K_{\rm pudc}+K_{\rm iudc}/(j\omega) \tag{a21}$$

$$G_{i\rm cm}(\omega)=-\left[K_{\rm picm}+\frac{2\omega_c K_{ri\rm cm}j\omega}{(j\omega)^2+2\omega_c j\omega+\omega_r^2}\right] \tag{a22}$$

$$G_i(\omega)=-\left[K_{\rm piac}+K_{\rm iiac}/(j\omega)\right] \tag{a23}$$

where $u_{\rm ac1}e^{\pm j\varphi}$ could be obtained from Table V, that is $u_{\rm ac1}e^{\pm j\varphi}=178\ 890\angle\mp 0.5°$; and negative signs in (a22) and (a23) guarantee the logic of these control loops. The transfer functions can be transformed into HSS by the method presented in Section IV, expressed as

$$\mathbf{G}_{\rm PLL}=\begin{bmatrix}0&0&0&0&0\\4.6\angle 125.5°&0&4.6\angle -54.4°&0&0\\0&0&0&0&0\\0&0&0&0&0\\0&0&0&0.57\angle 5.7°&0\end{bmatrix}\times 10^{-6} \tag{a24}$$

$$\mathbf{G}_{u\rm dc}=\mathrm{diag}\left(5\angle 0.2°,5\angle 0.9°,5\angle -0.2°,5\angle -0.1°,5\angle 0.1°\right)\times 10^{-3} \tag{a25}$$

$$\mathbf{G}_{i\rm cm}=-\mathrm{diag}\left(7.9\angle -49°,5\angle -7.3°,5.9\angle 31°,31\angle 72.2°,10.7\angle -59.6°\right)\times 10^{-5} \tag{a26}$$

$$\mathbf{G}_{i}=-\mathrm{diag}\left(1\angle 6.1°,1.2\angle 32.5°,1\angle -9°,1\angle -4.1°,1\angle -2.6°\right)\times 10^{-4}. \tag{a27}$$

According to the block diagram shown in Fig. 5, to get the HSS model of MMC controllers, $\mathbf{i}'_{d+}$, $\mathbf{i}'_{q+}$, $\mathbf{m}'_{d-}$, and $\mathbf{m}'_{q-}$ are still needed. It can be found from (29) that

$$[i'_{d+},i'_{q+}]^{\rm T}=T_{dq+}(\omega_1 t+90°)\,[i_{\rm acA},i_{\rm acB},i_{\rm acC}]^T \tag{a28}$$

by which i'_{d+} and i'_{q+} are solved as 11.2 and -1484.8 A, respectively. Similarly, from (36), we have

$$[m_{\rm dmA},m_{\rm dmB},m_{\rm dmC}]^{\rm T}=T_{dq-}(\omega_1 t+90°)\,[m'_{d-},m'_{q-}]^T. \tag{a29}$$

And m'_{d-} and m'_{q-} are solved as $0.43\cos(\omega_1 t+88.1°)$ and $0.02\cos(\omega_1 t-1.9°)$, respectively. Then, $\mathbf{i}'_{d+}$, $\mathbf{i}'_{q+}$, $\mathbf{m}'_{d-}$ and $\mathbf{m}'_{q-}$ could be obtained by transforming i'_{d+}, i'_{q+}, m'_{d-}, and m'_{q-} as Toeplitz matrix, that is

$$\mathbf{i}'_{d+}=\mathrm{diag}\left(11.2,11.2,11.2,11.2,11.2\right) \tag{a30}$$

$$\mathbf{i}'_{q+}=\mathrm{diag}\left(-1484.8,-1484.8,-1484.8,-1484.8,-1484.8\right) \tag{a31}$$

Finally, by substituting (a24)–(a33) into (47), the ac current response $\Delta i_{\rm ac}(\omega_p)$ under the closed-loop condition can be solved as $(7.6\angle -55.5°)$ A, which confirms the simulation results listed in Table III(a). And the MMC closed-loop ac impedance at 40 Hz is calculated as

$$Z_{\rm ac\_MMC}(\omega_p)=\frac{1000}{7.6\angle -55.5°}-(12+j48.8)=86.4\angle 43.6°. \tag{a34}$$

This is consistent with the closed-loop impedance curve shown in Fig. 6(e).

$$\mathbf{K}_{m\rm cm2}=\begin{bmatrix}0&6.8\angle -71.4°&0&0.09\angle 15.7°&0\\48\angle 89.1°&0&72.2\angle 90.4°&0&0.1\angle -171.6°\\0&45.5\angle -92°&0&5\angle -82.9°&0\\0.6\angle 173.3°&0&7.9\angle -87.6°&0&2.4\angle 81°\\0&0.2\angle -7.5°&0&8.9\angle -84.6°&0\end{bmatrix}\times 10^3 \tag{a13}$$

$$\mathbf{K}_{m\rm dm2}=\begin{bmatrix}411.9\angle 2.5°&0&29.1\angle 94.7°&0&0.001\angle 102°\\0&417.8\angle -7.5°&0&4\angle -76.8°&0\\23.8\angle 84.4°&0&417.2\angle 5°&0&0.3\angle -108.5°\\0&9.3\angle -91.6°&0&413.1\angle -0.4°&0\\0.001\angle 78°&0&5.6\angle -96.4°&0&413.2\angle 0.1°\end{bmatrix}\times 10^3. \tag{a14}$$

$$\mathbf{m}'_{d-} = \begin{bmatrix} 0 & \frac{0.43\angle -88.1^\circ}{2} & 0 & 0 & 0 \\ \frac{0.43\angle 88.1^\circ}{2} & 0 & \frac{0.43\angle -88.1^\circ}{2} & 0 & 0 \\ 0 & \frac{0.43\angle 88.1^\circ}{2} & 0 & \frac{0.43\angle -88.1^\circ}{2} & 0 \\ 0 & 0 & \frac{0.43\angle 88.1^\circ}{2} & 0 & \frac{0.43\angle -88.1^\circ}{2} \\ 0 & 0 & 0 & \frac{0.43\angle 88.1^\circ}{2} & 0 \end{bmatrix} \tag{a32}$$

$$\mathbf{m}'_{q-} = \begin{bmatrix} 0 & \frac{0.02\angle 1.9^\circ}{2} & 0 & 0 & 0 \\ \frac{0.02\angle -1.9^\circ}{2} & 0 & \frac{0.02\angle 1.9^\circ}{2} & 0 & 0 \\ 0 & \frac{0.02\angle -1.9^\circ}{2} & 0 & \frac{0.02\angle 1.9^\circ}{2} & 0 \\ 0 & 0 & \frac{0.02\angle -1.9^\circ}{2} & 0 & \frac{0.02\angle 1.9^\circ}{2} \\ 0 & 0 & 0 & \frac{0.02\angle -1.9^\circ}{2} & 0 \end{bmatrix} \tag{a33}$$

REFERENCES

[1] A. Lesnicar and R. Marquardt, "An innovative modular multilevel converter topology suitable for a wide power range," in *Proc. IEEE Power Technol. Conf.*, Bologna, Italy, Jun. 2003, vol. 3, pp. 1–6.

[2] S. Debnath, J. Qin, B. Bahrani, M. Saeedifard, and P. Barbosa, "Operation, control, and applications of the modular multilevel converter: A review," *IEEE Trans. Power Electron.*, vol. 30, no. 1, pp. 37–53, Jan. 2015.

[3] J. I. Leon, S. Vazquez, and L. G. Franquelo, "Multilevel converters: Control and modulation techniques for their operation and industrial applications," *Proc. IEEE*, vol. 105, no. 11, pp. 2066–2081, Nov. 2017.

[4] F. Rong, X. Gong, and S. Huang, "A novel grid-connected PV system based on MMC to get the maximum power under partial shading conditions," *IEEE Trans. Power Electron.*, vol. 32, no. 6, pp. 4320–4333, Jun. 2017.

[5] G. Tang *et al.*, "Basic topology and key devices of the five-terminal DC grid," *CSEE J. Power Energy Syst.*, vol. 1, no. 2, pp. 22–35, Jun. 2015.

[6] J. Lyu, X. Cai, M. Amin, and M. Molinas, "Sub-synchronous oscillation mechanism and its suppression in MMC-based HVDC connected wind farms," *IET Gener. Transmiss. Distrib.*, vol. 12, no. 4, pp. 1021–1029, Feb. 2018.

[7] C. Zou et al., "Analysis of resonance between a VSC-HVDC converter and the AC grid," *IEEE Trans. Power Electron.*, vol. 33, no. 12, pp. 10157–10168, Dec. 2018.

[8] Q. Hao, Z. Li, F. Gao, and J. Zhang, "Reduced-order small-signal models of modular multilevel converter and MMC-based HVDC grid." *IEEE Trans. Ind. Electron.*, vol. 66, no. 3, pp. 2257–2268, Mar. 2019.

[9] A. Antonopoulos, L. Ängquist, L. Harnefors, K. Ilves and H. P. Nee, "Global asymptotic stability of modular multilevel converters," *IEEE Trans. Ind. Electron.*, vol. 61, no. 2, pp. 603–612, Feb. 2014.

[10] X. Wang and F. Blaabjerg, "Harmonic stability in power electronic-based power systems: Concept, modeling, and analysis," *IEEE Trans. Smart Grid*, vol. 10, no. 3, pp. 2858–2870, May 2019.

[11] J. Sun, "Small-signal methods for AC distributed power systems—A review," *IEEE Trans. Power Electron.*, vol. 24, no. 11, pp. 2545–2554, Nov. 2009.

[12] L. Harnefors, A. Antonopoulos, S. Norrga, L. Angquist, and H. P. Nee, "Dynamic analysis of modular multilevel converters," *IEEE Trans. Ind. Electron.*, vol. 60, no. 7, pp. 2526–2537, Jul. 2013.

[13] M. Cespedes and J. Sun, "Impedance modeling and analysis of grid-connected voltage-source converters," *IEEE Trans. Power Electron.*, vol. 29, no. 3, pp. 1254–1261, Mar. 2014.

[14] Y. Li et al., "Modeling and damping control of modular multilevel converter based DC grid," *IEEE Trans. Power Syst.*, vol. 33, no. 1, pp. 723–735, Jan. 2018.

[15] N. M. Wereley and S. R. Hall, "Frequency response of linear time periodic systems," in *Proc. 29th IEEE Conf. Decis. Control*, 1990, vol. 6, pp. 3650–3655.

[16] N. M. Wereley and S. R. Hall, "Linear time periodic systems: Transfer function, poles, transmission zeroes and directional properties," in *Proc. Amer. Control Conf.*, 1991, pp. 1179–1184.

[17] N. M. Wereley, "Analysis and control of linear periodically time varying systems," Ph.D. dissertation, Massachusetts Inst. Technol., Cambridge, MA, USA, 1991.

[18] G. Love, "Small signal modelling of power electronic converters, for the study of time domain waveforms, harmonic domain spectra, and control interactions," Ph.D. dissertation, Univ. Canterbury, Christchurch, New Zealand, 2007.

[19] J. Kwon, X. Wang, F. Blaabjerg, C. L. Bak, V.-S. Sularea, and C. Busca, "Harmonic interaction analysis in a grid-connected converter using harmonic state-space (HSS) modeling," *IEEE Trans. Power Electron.*, vol. 32, no. 9, pp. 6823–6835, Sep. 2017.

[20] X. Yue, X. Wang, and F. Blaabjerg, "Review of small-signal modeling methods including frequency-coupling dynamics of power converters," *IEEE Trans. Power Electron.*, vol. 34, no. 4, pp. 3313–3328, Apr. 2019.

[21] A. Jamshidifar and D. Jovcic, "Small-signal dynamic DQ model of modular multilevel converter for system studies," *IEEE Trans. Power Del.*, vol. 31, no. 1, pp. 191–199, Feb. 2016.

[22] J. Sun and H. Liu, "Sequence impedance modeling of modular multilevel converters," *IEEE J. Emerg. Sel. Topics Power Electron.*, vol. 5, no. 4, pp. 1427–1443, Dec. 2017.

[23] J. Lyu, X. Cai, and M. Molinas, "Optimal design of controller parameters for improving the stability of MMC-HVDC for wind farm integration," *IEEE J. Emerg. Sel. Topics Power Electron.*, vol. 6, no. 1, pp. 40–53, Mar. 2018.

[24] J. Lyu, X. Zhang, X. Cai, and M. Molinas, "Harmonic state-space based small-signal impedance modeling of a modular multilevel converter with consideration of internal harmonic dynamics," *IEEE Trans. Power Electron.*, vol. 34, no. 3, pp. 2134–2148, Mar. 2019.

[25] H. Wu, X. Wang, and Ł. Kocewiak, "Impedance-based stability analysis of voltage-controlled MMCs feeding linear AC systems," *IEEE J. Emerg. Sel. Topics Power Electron.*, early access, doi: 10.1109/JESTPE.2019.2911654.

[26] Z. Xu, B. Li, S. Wang, S. Zang, and D. Xu, "Generalized single-phase harmonic state space modeling of the modular multilevel converter with zero-sequence voltage compensation," *IEEE Trans. Ind. Electron.*, vol. 66, no. 8, pp. 6416–6426, Aug. 2019.

[27] Y. Ma, H. Lin, and Z. Wang, "Equivalent model of modular multilevel converter considering capacitor voltage ripples," *IEEE Trans. Power Del.*, vol. 34, no. 6, pp. 2182–2193, Dec. 2019.

[28] K. Ji, G. Tang, H. Pang, J. Yang, "Impedance modeling and analysis of MMC-HVDC for offshore wind farm integration," *IEEE Trans. Power Del.*, vol. 35, no. 3, pp. 1488–1501, Jun. 2020.

[29] K. Ji, G. Tang, J. Yang, Y. Li, and D. Liu, "Harmonic stability analysis of MMC-based DC system using dc impedance model," *IEEE J. Emerg. Sel. Topics Power Electron.*, vol. 8, no. 2, pp. 1152–1163, Jun. 2020.

[30] H. Gong, D. Yang, and X. Wang, "Identification of the DQ impedance model for three-phase power converter considering the coupling effect of the grid impedance," in *Proc. IEEE Appl. Power Electron. Conf. Expo.*, Anaheim, CA, USA, 2019, pp. 120–126.

[31] X. Wang, L. Harnefors, and F. Blaabjerg, "Unified impedance model of grid-connected voltage-source converters," *IEEE Trans. Power Electron.*, vol. 33, no. 2, pp. 1775–1787, Feb. 2018.
[32] I. Vieto and J. Sun, "Sequence impedance modeling and converter-grid resonance analysis considering DC bus dynamics and mirrored harmonics," in *Proc. IEEE 19th Workshop Control Model. Power Electron.*, Padua, Italy, 2018, pp. 1–8.
[33] H. Wu and X. Wang, "Dynamic impact of zero-sequence circulating current on modular multilevel converters: Complex valued AC impedance modeling and analysis," *IEEE J. Emerg. Sel. Topics Power Electron.*, vol. 8, no. 2, pp. 1947–1963, Jun. 2020.
[34] L. Bessegato, K. Ilves, L. Harnefors, and S. Norrga, "Effects of control on the AC-side admittance of a modular multilevel converter," *IEEE Trans. Power Electron.*, vol. 34, no. 8, pp. 7206–7220, Aug. 2019.
[35] Y. Sun, C. A. Teixeira, D. G. Holmes, B. P. McGrath, and J. Zhao, "Low-order circulating current suppression of PWM-based modular multilevel converters using DC-link voltage compensation," *IEEE Trans. Power Electron.*, vol. 33, no. 1, pp. 210–225, Jan. 2018.

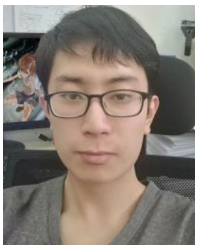

Zigao Xu (Student Member, IEEE) received the B.S. degree in electrical engineering from the Taiyuan University of Technology, Taiyuan, China, in 2016, and the M.S. degrees in 2018 from the Harbin Institute of Technology, Harbin, China, where he is currently working toward the Ph.D. degree.

His research interests include multilevel converters, modeling, and control.

Binbin Li (Member, IEEE) received the B.S., M.S., and Ph.D. degrees in electrical engineering from the Harbin Institute of Technology, Harbin, China, in 2010, 2012, and 2017, respectively.

From 2015 to 2016, he was a Visiting Researcher with the Department of Electronic and Electrical Engineering, University of Strathclyde, Glasgow, U.K. He is currently an Associate Professor with the Department of Electrical Engineering, Harbin Institute of Technology. He has also been selected in the Young Elite Scientists Sponsorship Program by China Association for Science and Technology. His research interests include modular power converters, HVdc grid, and MVdc collection/distribution system.

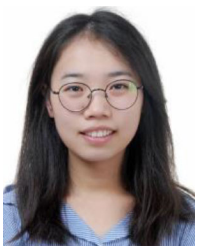

Linjie Han received the B.S. degree in electrical engineering from Beijing Jiaotong University, Beijing, China, in 2019. She is currently working toward the M.S. degree with the Harbin Institute of Technology, Harbin, China.

Her research interests include multilevel converters and power hardware-in-the-loop.

Junlin Hu received the B.S. degree in electrical engineering from Shijiazhuang Tiedao University, Shijiazhuang, China, in 2019. He is currently working toward the M.S. degree with the Harbin Institute of Technology, Harbin, China.

His research interests include modular multilevel converter and power amplifier used in power hardware-in-the-loop.

Shengbo Wang (Student Member, IEEE) received the B.S. degree in electrical engineering in 2018 from the Harbin Institute of Technology, Harbin, China, where she is currently working toward the M.S. degree.

Her research interests include multilevel converters and modeling.

Shiguang Zhang received the B.S. degree in electrical engineering from Anhui University, Anhui, China, in 2018. He is currently working toward the M.S. degree with the Harbin Institute of Technology, Harbin, China.

His research interests include multilevel converters and modeling and control.

Dianguo Xu (Fellow, IEEE) received the B.S. degree in control engineering from Harbin Engineering University, Harbin, China, in 1982, and the M.S. and Ph.D. degrees in electrical engineering from the Harbin Institute of Technology (HIT), Harbin, China, in 1984 and 1989, respectively.

In 1984, he joined as an Assistant Professor with the Department of Electrical Engineering, HIT, where he has been a Professor since 1994. He was the Dean of School of Electrical Engineering and Automation, HIT, from 2000 to 2010. He is currently the Vice President of HIT. He has authored/coauthored more than 600 technical papers. His research interests include renewable energy generation technology, multiterminal HVdc system based on VSC, power quality mitigation, speed sensorless vector controlled motor drives, and high-performance servo system.

Prof. Xu is an Associate Editor for the IEEE TRANSACTIONS ON INDUSTRIAL ELECTRONICS, IEEE TRANSACTIONS ON POWER ELECTRONICS, and the IEEE JOURNAL OF EMERGING AND SELECTED TOPICS IN POWER ELECTRONICS. He also serves as the Chairman of IEEE Harbin Section.